REPORT DOCUMENTATION PAGE

AFRL-SR-BL-TR-00-

0063

1. REPORT DATE (DD-MM-YYYY) 01-09-2000	2. REPORT TYPE Final Report	3. DATES COVERED (From - To) 01-02-1998 31-08-2000

4. TITLE AND SUBTITLE
Investigation of Combined Low-Angled Jets and Variable Wall

Geometry for Hypersonic Aerodynamic Control

5a. CONTRACT NUMBER
F49620-98-1-0336

5b. GRANT NUMBER

5c. PROGRAM ELEMENT NUMBER

6. AUTHOR(S)
Rodney D. W. Bowersox, Dr.

Huaiguo Fan, Mr.

5d. PROJECT NUMBER

5e. TASK NUMBER

5f. WORK UNIT NUMBER

7. PERFORMING ORGANIZATION NAME(S) AND ADDRESS(ES)

The University of Alabama
Aerospace Engr. & Mechanics
Box 870280
Tuscaloosa, AL 35487

8. PERFORMING ORGANIZATION REPORT NUMBER

UA-AEM-APL-2000-001

9. SPONSORING / MONITORING AGENCY NAME(S) AND ADDRESS(ES)
AFOSR/NA
801 N. Randolph St., Rm. 732
Arlington, VA 22203-1977

10. SPONSOR/MONITOR'S ACRONYM(S)

11. SPONSOR/MONITOR'S REPORT NUMBER(S)

12. DISTRIBUTION / AVAILABILITY STATEMENT
Approved for Public Release; Distribution Unlimited

DTIC QUALITY INSPECTED 4

20001208 055

13. SUPPLEMENTARY NOTES

14. ABSTRACT
A comprehensive investigation of the use of low-angled jets to control the aerodynamic forces, viscous drag, and heat transfer for hypersonic vehicles was performed. The research program was divided into two thrusts. The first thrust involved construction of a new experimental hypersonic research laboratory. The laboratory houses two wind tunnels (a Mach 5.0 blow-down and a Mach 7.0 shock tunnel) developed as part of this project. The second thrust concentrated on examining the flow features of sonic injection into a hypersonic (Mach 5.0), high-Reynolds number ($Re/m = 55\times10^6$) cross-flow for flow field understanding, predictability, and controllability. With this understanding, improved variable wall plume control devices can be developed to increase the film cooling and boundary layer control effectiveness of the jets. The use of a distributed-array of multiple jets for thermal protection and separation control was also investigated. A two-year program was performed.

15. SUBJECT TERMS
Hypersonic Flow, Jet-Into-A-Cross-flow, Reaction Control, Vorticity, Turbulence, Separation

16. SECURITY CLASSIFICATION OF:			17. LIMITATION OF ABSTRACT	18. NUMBER OF PAGES	19a. NAME OF RESPONSIBLE PERSON Rodney Bowersox
a. REPORT Unclassified	b. ABSTRACT Unclassified	c. THIS PAGE Unclassified	SAR		19b. TELEPHONE NUMBER (include area code) (205)348-1905

Standard Form 298 (Rev. 8-98)
Prescribed by ANSI Std. Z39.18

INVESTIGATION OF COMBINED LOW-ANGLED JETS AND VARIABLE WALL GEOMETRY FOR HYPERSONIC AERODYNAMIC CONTROL

FINAL REPORT

Dr. Rodney D. W. Bowersox
Mr. Huaiguo Fan
Department of Aerospace Engineering and Mechanics
The University of Alabama
Box 870280
Tuscaloosa, AL 35487

Executive Summary

This document summarizes the results from a very successful two-year study with two objectives, one developing new hypersonic test capabilities and two improving the understanding of the complicated flow field created by injection into a hypersonic cross-flow. The Air Force applications include reaction control, thermal protection, separation control and fuel injection for advanced vehicles including accelerators (missiles), maneuvering re-entry vehicles, rapid response global reach aircraft systems, and space launch support accelerators. The research program was divided into two main thrusts associated with each objective.

The hypersonic laboratory development thrust was very successful. A Mach 5.0 blow-down tunnel was designed and constructed, and has been run over eight hundred times for this project. This facility is relatively unique and offers a low-cost national wind tunnel resource for basic hypersonic flow research, and with the recent upgrades, fifteen hundred runs per year are anticipated. A large-scale, high-energy shock tunnel facility was designed, and construction will be completed this year. This facility is also relatively unique. A detailed description of each facility is presented in Chapter 3.

The second thrust was also very successful, where a new and extensive database for single-port sonic injection into a hypersonic (M = 5.0), high Reynolds number (Re/m = 55 x 10^6) cross-flow was developed. To provide a broad database, injector conditions were tested. In addition, to provide complete flow field documentation, numerous experimental techniques were employed. A multi-port distributed-array-injector was

designed based on the single-port database, and studied. In addition, the use of variable wall geometry for plume vorticity control was examined. Detailed flow field descriptions for the various cases were discerned, and numerous pragmatic flow field conclusions have been drawn. Of particular interest was the observation that the hypersonic jet-interaction did not possess the usual characteristics depicting a strong counter rotating vortex pair. This finding has important theoretical implications toward control and prediction, and numerous factors were deemed important toward producing the apparent low levels of plume vorticity.

Two technology transfers have occurred because of this project. Specifically, the PI is working closely with the Air Force Research Laboratory to incorporate the diamond injector technology into current scramjet combustion development efforts, and the PI, as part of the follow-on research project, is examining, with strong interaction with NASA Langley, the use of diamond injectors for roll control of the X-43 flight test vehicle. In addition, the PI used the single-port database to design a distributed-array-injector plate for shock induced boundary layer separation control.

Recommendations for follow-on research include examination of additional injector shapes to better quantify the role of the recompression shock on the plume vorticity generation. The distributed array concept demonstrated promise, however additional work is required to fully examine the possibilities. Lastly, it is recommended that the single-port database be extended to include both dissimilar and reacting gaseous injection, and because of the rugged stainless steel construction, the new Mach 5.0 tunnel is uniquely appropriate for this.

List of Symbols

A_j Injector Exit Port Area

A_p Plume Area

d Effective Jet Diameter for the Single-Port-Injector [$=(4A_j/\pi)^{1/2} = 4.89$ mm]

d_d Effective Jet Diameter for the Distributed-Array-Injector (= 2.2 mm)

J Jet-to-Free stream Momentum Ratio ($=\rho_j u_j^2 / \rho_\infty u_\infty^2$)

M Mach Number

p Static Pressure

p_{eff} Effective Back Pressure

p_t Total Pressure

Re/m Unit Reynolds Number

T Static Temperature

T_t Total Temperature

u Axial Velocity

x, y, z Cartesian Coordinates

y_{max} Maximum Plume Penetration

α Injector Incidence Angle

ρ Density

τ_{ij}^{T} Turbulent Shear Stress

Subscripts

j Injector Condition

∞ Free Stream Condition

1   Flow Condition Upstream Shock

2   Flow Condition Downstream of Shock

List of Tables

List of Figures

Table of Contents

Chapter 1

Introduction

1.1 Documented Air Force Requirements

"Sustained hypersonic flight offers potential revolutionary improvements in future war-fighting and space launch capabilities. ... Hypersonic speeds greatly enhance both survivability and [lethality] by practically eliminating enemy defensive capabilities. (*New World Vistas*, 1995)." These quotes from the Air Force *New World Vistas* (1995) clearly define the importance of hypersonic flight to the future of the US Air Force. The potential future Air Force vehicles listed in the document include accelerators (missiles), maneuvering re-entry vehicles, rapid response global reach aircraft systems, and space launch support accelerators. The aerodynamic technology requirements for these hypersonic vehicles include improving lift-to-drag ratios, developing shapes that minimize aerodynamic heating, developing rapid and precise aerodynamic control systems, and propulsion integration (*New World Vistas*, 1995). In addition to these aerodynamic requirements, radar cross-section reduction is also an important factor that will influence the development of future Air Force weapon systems. The present research is directly applicable to the above documented Air Force requirements. Specific technology transitions are described in Section 1.5.

1.2 Research Concept and Problem Statement

1.2.1 Thrust 1 – Hypersonic Research Laboratory Development

As the previous section indicated, hypersonic vehicles have important Air Force missions. Unfortunately, ground test capabilities have significantly dwindled over the past three decades [*New World Vistas* (1995)], and consequently the resources in the test community are new very limited. Hence, a large portion of this research program was devoted toward developing a new research laboratory for basic hypersonic research. First, a small-scale Mach 5.0 wind tunnel specifically designed for basic research was proposed. This tunnel is one of two such operational university facilities in the country. Second, a large-scale, high-energy hypervelocity shock tunnel was proposed. This facility is also one of two or three in universities across the United States. Third, it was also proposed to extend numerous modern flow field diagnostic techniques, such as digital two-color particle image velocimetry and multiple overheat cross-wire anemometry, to the hypersonic flow regime to provide high-resolution (both spatially and temporally) data for improved flow field understanding.

1.2.2 Thrust 2 – Hypersonic Jet Interaction

Jets can be very effective rapid reaction control devices for hypersonic vehicles. One advantage of a reaction control jet over a control surface is the elimination of a

thermally protected control surface. However, as discussed in Chapter 2, numerous complicated vortical flow features characterize a jet into a cross-flow, and modern physical models are not accurate.

Jets are also effective for film cooling thermal protection. A Mach 8 vehicle will experience wall temperatures on the order of 2,700K. The only metals that can survive these temperatures are very heavy (e.g., Tungsten is nearly ten times heavier than Titanium). Thus, the aerosurfaces will require thermal protection (either ceramics or film cooling). One of the distinguishing characteristics of a jet into a cross-flow is the strong counter-rotating vortex pair within the plume (see Chapter 2 for a detailed flow field description). This counter rotating vortex pair has an adverse influence on the film cooling effectiveness, where the vortex pair interacts with the surface causing the jet plume to lift-off the surface via the Magnus force. In a recent study aimed at improving the penetration of a jet into a supersonic cross-flow, our group investigated the use of small ramps placed just downstream of the injector port [Wilson, Bowersox and Glawe (1998)]. The ramps were designed to interact with the counter-rotating vortex pair, and thus increase the penetration via the Magnus force. Our team discovered that by varying the ramp geometry the plume vorticity could be controlled. One ramp configuration reduced the vorticity within the plume to the level of being undetectable, and our numerical simulations [Chenault, Beran and Bowersox (1999)] indicated that the recompression shock (described in Chapter 2) is a main vorticity production mechanism. Hence, the most likely case for the plume vorticity control is that the ramps reshape the recompression shock. Once the flow processes are better understood, methodologies that

range from simple fixed ramps to sophisticated nonlinear adaptive control using micro-electrical-mechanical systems (MEMS) can be developed to control the jet plume features including plume axial vorticity.

Although the counter-rotating vortex pair can have a negative impact on film cooling, this characteristic has the potential to be an effective means of boundary layer control. It is expected that the axial vorticity within the jet plume can be used to energize the lower portion of the boundary layer with the goal of reducing wall pressure fluctuations by extending the axial length of the "U-vortex" described in Hinze (1975). Low-speed experimental data indicate that the wall shears stress is linearly proportional to the root-mean-square wall pressure fluctuations (Hinze, 1975). Hence, the reduced wall pressure fluctuations will result in reduced momentum loss (skin friction). Energizing the boundary layer can also be used to increase the resistance of the boundary layer to shock induced separation.

In summary, the understanding and predictability of a jet into a cross-flow, especially at high-speeds, is limited by the extreme dearth of experimental studies (Chapter 2 describes in detail the current limitations). However, as discussed Chapter 2, recent advances in experimental methods allow for in depth studies directed at understanding the flow physics. The better flow field understanding, produced in this study, provides engineers and scientists the requisite information to capitalize on the jet flow features to enhance the performance of hypersonic systems.

1.3 Research Objectives and Approach

This research project had two principal objectives. The first objective was the development of a research laboratory to provide high-quality, low-cost hypersonic test capability. The second objective was to use this new laboratory to improve the understanding and prediction capability of the combined use of low-angled jets and variable wall geometry to control the aerodynamic forces, viscous drag, and heat transfer for hypersonic vehicles.

In order to meet the research objectives, the research program was divided into two main thrusts. The first thrust of the program focused on the development of the experimental research laboratory to perform the basic hypersonic flow research. The second main thrust of this project concentrated on examining the flow features of sonic injection, over range of injector configurations and condition, into a hypersonic cross-flow for flow field understanding, predictability, and controllability. In addition, the use of an array of distributed jets for boundary layer separation control was also investigated. An overview of the research approach for each phase of the project is discussed below.

A new Mach 5.0 basic research blow-down wind tunnel was designed, constructed and calibrated. A complete description is presented in Chapter 3. In addition, a large-scale hypersonic (M = 5.0 and 7.0) true flight enthalpy impulse tunnel was designed and construction is nearly completed; this tunnel will be completed this year with funding from a follow-up research grant from the AFOSR. Table 1.1 lists the flow conditions for both facilities. In addition, the necessary apparatus, such as schlieren

photography, data acquisition, particle image velocimetry, hot-wire anemometry, five-hole-probe, etc ..., (Chapter 3) were also established. These two facilities are relatively unique in the university community and they provide a high quality, low-cost national resource for basic hypersonic flow research.

A comprehensive mean flow database for single port diamond injection into a Mach 5.0 cross flow was produced. Shown in Fig 1a is a schematic of the injectors. Diamond orifices were chosen over conventional circular injectors because of the possibility of attached shock waves for the diamond shapes that translated into reduced total pressure loss (i.e., less drag). In addition, attached shocks eliminate the upstream flow separation and subsequent high heating rate associated with conventional injection. Five diamond shaped orifice incidence angles (10 - 135°), a 90° circular injector, and a variable wall geometry vortex generation ramp, based on the work of Wilson, Bowersox and Glawe (1998), were tested. A broad range of injector conditions (Table 1.2) was tested to provide information for engineering decisions. The experimental methods used included particle image velocimetry, Pitot/cone-static pressure, pressure sensitive paint, Mie-scattering flow visualizations, and surface oil flow visualizations. This list of experimental methods was selected to provide a complete understanding of the mean flow field.

As mentioned above, one application of the present work is the use of jets is to add stream wise vorticity to the boundary layer with the goal of strengthening the boundary layer resistance to separation. The basic idea was to use a distributed-array of small jets (Fig 1.1b shows a schematic) to form layers of "vortex sheets," where the flow

field for each individual jet (as discussed in Chapters 2 and 4) is dominated by axial vorticity. Hence, the distribution of jets was used to produce a layer within the boundary layer dominated by axial vorticity. Figure 1.2 shows a schematic of the concept. The jet lateral spacing was chosen such jet-interaction was incipient. The purpose of this spacing was twofold. First, the jet vorticity layer would be roughly uniform in the lateral direction. Second, the incipient interaction produces curved isotachs. Curved isotachs also produce axial corner flow vorticity [Gessner (1973)]. Hence, as indicated in Fig. 1.2, the distributed-array model was designed to produce numerous layers of vorticity across the boundary layer. The specific model design is described in Chapter 3. The experimental techniques used here include the five-hole pressure probe, surface oil flow visualization and color schlieren photography.

1.4 Research Timeline and Progress

A two-year research project was performed. A timeline for the research project is given in Table 1.3. Upon receipt of funding, Dr. Bowersox and a department supported graduate student immediately began construction of the Mach 5.0 wind tunnel (Chapter 3 describes facilities). However, an unforeseen delay due to asbestos removal was incurred. The asbestos removal delayed the construction of the new Hypersonics Laboratory by approximately ten months. During this period, the pebble heater was constructed, and the diamond injector models were designed and constructed as described in Chapter 3. Because of the asbestos delay, a generous six-month no-cost extension was

granted by the AFOSR. Thus, the net loss in time to the project was approximately four months. After entry into the laboratory, the Mach 5.0 wind tunnel construction was completed and testing began. As Table 1.3 indicates, the project, once begun, progressed at an accelerated pace, and approximately 90% of the work was completed. The remaining work is currently underway and will be completed as part of the follow-on grant.

The Mach 5.0 wind tunnel operation was very smooth. To date, we have run the tunnel nearly eight hundred times, which required very long shifts in the laboratory. In order to speed up the experimental process, we purchased a second compressor (October 2000) at no additional cost to the project to speed-up the pump-up time (currently, four hours) by a factor of two, and to provide redundancy in the system to help eliminate down periods. It is anticipated that with this upgrade, along with a new pre-heater (described in Chapter 3), the number runs per year will increase to approximately fifteen hundred.

Mean flow data for the single-port-injectors listed in Table 1.2 were acquired and analyzed (Chapter 4). Analysis of the five-hole-probe data indicated that a low-Reynolds number calibration of the cross-wire probes was required. Hence, a new calibration facility, which was unforeseen in the original proposal, was required. The facility was designed, constructed and calibrated (as described in Chapter 3).

The distributed-array model was designed, constructed (Chapter 3) and tested. Surface oil flow visualization, color schlieren photographs and detailed five-hole-probe data were acquired and analyzed (Chapter 4).

Important items in Table 1.3 are still in-progress; namely, the turbulence measurements with the cross-wire probe for the single-port models and the turbulence modeling/numerical effort. These efforts are continuing with funding from the follow-on project. In order to make-up lost time, a second MS student recently joined the project at no additional cost to AFOSR. This student began working on the computational modeling for this project, and preliminary simulations with current turbulence models were accomplished (Chapter 4).

The shock tunnel design and construction proceeded at very good pace. The shock tube pipe was fitted with flanges (in-house); stands were designed and constructed in-house, and the tube was mounted. The shock tunnel is described in Chapter 3. The nozzles (Mach 7 and 5) were mounted and the vacuum receiver was purchased and tested. The primary diaphragm holder was designed, the materials were purchased, and construction has begun. Once the primary diaphragm holder is constructed, recoil measurements will be acquired and the secondary diaphragm holder, which will require a custom slip joint, will be designed and constructed. This effort will continue under the follow-on grant with a new PhD student from the Air Force Academy.

1.5 Scientific Impact and Technology Transitions

The first thrust of this research project resulted in a new hypersonic research laboratory that provides a high quality, low cost test capability. The second thrust has provided a full characterization of the mean flow physics of a single port jet into a

hypersonic cross-flow. As discussed in Sections 1.2 and 1.3, this database can have a large impact on future hypersonic vehicles. This portion of the research provides engineers with the data and understanding necessary to use injection to improve the performance of future hypersonic vehicles (reaction control jets, film cooling, boundary layer control, and perhaps electromagnetic cross-section reduction). In addition, the use of distributed jets for boundary layer separation was examined, and a distributed-array scheme was developed. Specific Air Force technology transitions are listed below.

Two specific Air Force technology transitions occurred as a direct result of this project. First, the Air Force Research Laboratory High-Speed Propulsion Division is now investigating the use of diamond jets for supersonic combustion ramjet (scramjet) primary fuel injectors. In addition, they are also examining the use of the distributed-array for separation control in the scramjet isolator. The PI is working closely with the Air Force on both of these transitions. Second, the follow-on AFOSR research project is being performed with close collaboration with NASA Langley Research Center. Specifically, NASA is interested in the use of jets for roll control on the X-43 research vehicle.

1.6 Deliverables

The results of this research program were disseminated to the US Air Force and aerospace industry through this contractor report, archival journal publications and presentations at national conferences.

1.7 Personnel

Dr. Rodney D. W. Bowersox, Associate Professor of Aerospace Engineering at The University of Alabama, was the lead PI on this project. The primary graduate research assistant on this project was Mr. Huaiguo Fan, a PhD candidate in the Department of Aerospace Engineering and Mechanics at the University of Alabama. Secondary graduate support for the preliminary numerical predictions was provided Mr. Saleh Al-Dughayem at no additional cost to the AFOSR. Mr. Steven Hudson provided additional laboratory support as an Undergraduate Engineering Scholar funded by the College of Engineering at the University of Alabama.

Chapter 2

Jet-Interaction Background Review

2.1 Jet-Into-A-Cross-flow

Injection into a cross-flow is a fundamentally important flow field that has implications across a myriad of military and civil disciplines. Thus, numerous experimental studies, primarily at low-speeds, have been performed to quantitatively assess the mean flow field and qualitatively examine the instantaneous vortical flow features [for example, Margason (1993), Kuethe (1935), and Kamotani and Greber (1972)]. However, studies that contain turbulence data suitable for flow field understanding are exceedingly scarce [Margason (1993)]. Furthermore, the available mean and turbulence data for supersonic flows are also limited. However, some studies were found, and the results of which are integrated into the following the discussions. Hypersonic jet-interaction studies are virtually non-existent.

Injection into a low-speed cross-flow produces a complex flow with at least four distinguishable vortical flow characteristics (see Fig. 2.1). As the jet emerges into the cross-flow, it is curved downstream by the cross-flow. The jet plume cross-section evolves into a cardioidal or "kidney-bean" shape. The counter-rotating vortex pair within the plume is responsible for the distorted plume shape. A number of flow mechanisms are responsible for generating this secondary flow. For example, turning of the flow into the downstream direction creates a pressure gradient across the flow that induces vortical

motion. Lateral shearing along the plume edges also contributes to the vorticity. The jet-free stream interaction (separation) creates a horseshoe vortex similar to that of a wing-body junction on an aircraft. The third vortex system consists of jet-shear layer vortices. Lastly, a fourth wake vortex system exists. Until recently, the formation of this unsteady vortex phenomenon had been attributed to vortex shedding similar the Karman-vortex wake of a cylinder in a cross-flow. Because Fric and Roshko (1994) were only able to visualize this system when the boundary layer was seeded with smoke, they reasoned that the vortices were the result of upstream boundary layer vorticity being transported up into the wake. The process is believed to be the result of "separation events" and eruptions of the boundary layer fluid and vorticity into "tornado-like" structures that begin at the wall and are entrained into the jet flow. Although Fric and Roshko present rather convincing evidence for this hypothesis, some contradicting evidence has also been presented. For example, the planar laser induced fluorescence concentration measurements of Lozano et al. (1994), show signs of the structures. However in that study, only the jet flow was seeded. Hence, these data may suggest that these structures could in part emanate from the jet and not the wall. Adding to this apparent dilemma, Kelso et al. (1993) present three possible scenarios leading to the formation of the wake vortex system. These unsteady phenomena can be very important for future flow control algorithms.

For high-speed flows, the mean flow features are similar to those described above. However, compressibility creates additional features that do not have incompressible counterparts. For example, perpendicular injection of an underexpanded sonic or supersonic jet into a supersonic free stream produces several flow structures. The first of

these is a bow shock produced as the free stream impacts the injection streamtube; in this respect the injectant acts as a solid cylindrical body [Hollo, McDaniel and Hartfield (1994)]. For injector configurations where injector diameter is greater than the boundary layer thickness, a separation bubble and a lambda shock form slightly upstream of the injector port [Schetz and Billig (1966)]. After entering the free stream, the jet experiences a rapid Prandtl-Meyer expansion (usually assumed to be an isentropic process) surrounded by a barrel shock [Grasso and Magi (1995)]. A shock normal to the jet path, known as the Mach disk, terminates the barrel shock, and compresses the flow to the appropriate (i.e., effective) back pressure. As the free stream flow wraps around the jet, a recompression shock is created. Recent CFD calculations by our team [Chenault, Beran and Bowersox (1999)] (see Fig. 2.2) indicate that the recompression shock creates an addition counter-rotating vortex pair that eventually engulfs the original jet induced pair discussed above.

Angled injection is a means of reducing total pressure loss. In either normal or angled injection, the entry of the injectant jet into the mainstream flow can be regarded as a two-stage process [Schetz and Billig (1966)]. The jet first enters the main flow and remains relatively intact as it expands to the height of the Mach disk. Beyond the Mach disk, the flow turns coaxial to, and accelerates with, the main flow. In the second stage, the jet acts as a coaxial vortex mixing structure. It is this feature that may be useful for boundary layer control (i.e., drag reduction).

During a rather extensive literature review, only a very limited number of studies on injection flows were found that included turbulence measurements. For low-speed

flows Andreopoulus and Rodi (1984), Fric and Roshko (1989), Kamotani and Greber (1972) were the only ones identified. For high-speed flows, the McCann and Bowersox (1996) and Bowersox (1996c) Mach 3.0 studies were the only ones located. This finding is consistent with that of the Margason (1993). Hence, the turbulent flow physics of the injection into a cross-flow are significantly less understood than their mean flow counterpart. However from the available data, some limited qualitative insight into the overall structure can be gleaned. For example the axial turbulence intensity contour plots of Kamotani and Greber (1972) indicated that two peaks in the intensity levels existed across the plume. In addition, the peaks were roughly co-located with each of the vortices of the counter rotating vortex pair. Investigating a high-speed angled injection case, McCann and Bowersox (1996) found that the turbulent kinetic energy also had two peaks, which were roughly, located just below each vortex with the vortex pair. They deduced that the increased strain rates due to the secondary vortex flow resulted in an increased production of the turbulent kinetic energy. The data of McCann and Bowersox also demonstrated that the x-y turbulent shear stresses peaked along the plume centerline, and the x-z shear stresses were highly asymmetrical. However, as suggested by Cantwell (General Discussion, 1993), the peak turbulence levels along the jet centerline may be the result of an unsteady movement of the vortex pair. It is also important to mention here that a number of experimental studies show an asymmetry in the mean flow. Further, the numerical simulation of a shocked jet (Drummond, 1996) also showed signs of an asymmetry. Bowersox (1996c) presents three possible scenarios to explain the generation of the asymmetry. The incompressible data of Andreopoulus and Rodi (1984)

15

presented the axial variation of the x-y and x-z turbulent shear stresses for two spanwise locations. Unfortunately, the spatial resolution of that study was sparse; hence, only limited quantitative information was available. However, those data showed trends in the turbulence decay rates. Though the limited data available in the literature, in conjunction with a current understanding of the mean flow field, can provide a qualitative impression of the turbulent flow structure, studies with enough detail for turbulence model development and validation are virtually non-existent. This conclusion is supported by the review of Margason (1993), and it was also the consensus during the General Discussion session following a recent AGARD meeting (General Discussion, 1993) among a number of key international researchers. Further, Chui et. al. (1993) and Alverez et al. (1993) both indicated that turbulence modeling was the limiting key factor in determining the accuracy of their numerical predictions. Hence, detailed experimental studies are required to develop turbulence models for design applications.

2.2 Overview of Current Prediction Methods and Empirical Database

Currently, engineers and scientists rely on an approximate form the governing equations of motion to predict the overall mean flow character of these flows. The Reynolds and Favre averaged forms of the Navier-Stokes equations are universally used to compute low-speed and high-speed flows, respectively.

Associated with the averaging procedure is the requirement for accurate turbulence models. Currently, industry standard eddy viscosity gradient transport

turbulence models, such as Baldwin-Lomax algebraic and k-ε/ω two equation, are extended to more complex flows on an *ad hoc* basis. However, as discussed in Wilcox (1993), current eddy viscosity models are not accurate for three-dimensional, vortex-dominated flows. As discussed in Section 2.1, the jet into a cross-flow flow field is dominated by numerous three-dimensional vortex systems; thus, the current prediction methods are not accurate.

In a recent numerical study of injection into a cross-flow, Chui et al. (1993) noted that the predictions of the flow with the eddy viscosity Baldwin-Lomax and Baldwin-Barth models "... compared no better with the experimental data than the laminar flow computation." Alverez et al. (1993) reported similar shortcomings. In a recent survey of 333 articles that covered a 50-year era, Margason (1993) concluded that there is a need for high quality, high fidelity experimental data that will allow for verification of current and future computational fluid dynamic results and to define the unsteady flow characteristics. Also, the during the General Discussion, following the 1993 AGARD (General Discussion, 1993) conference, entitled *Computational and Experimental Assessment of Jets in a Cross-flow*, there was some surprise that more detailed and high fidelity Laser Doppler and Particle Image Velocimetry data were not available for turbulence model development and evaluation.

2.3 Recent Advances in Technology that Allow for the Present Research

Modern advanced laser based experimental diagnostic techniques, such as particle

image velocimetry and pressure sensitive paint, allow for detailed and accurate measurements of the instantaneous mean, and turbulence statistics at high spatial resolution. In addition, modern computational resources, such as the University of Alabama Super Computer (described in Chapter 3), allow for routine simulation of complex three-dimensional flows.

2.4 Control of the Jet into a Cross-flow Using Variable Wall Geometry

In a recent research program focused on supersonic combustion applications, Wilson, Bowersox and Glawe (1998) placed small ramps just downstream of the exit port of a jet issuing into a high-speed cross-flow. The original motivation behind placing the ramps was to increase penetration via the Magnus force generated by interaction between the strong counter rotating vortex pair within the plume (Section 2.1 describes the flow features) and the ramp surfaces. That study was limited to one injector angle (25 degrees) at Mach 3.0. However, seven ramp configurations were tested. Because of the lack of design tools (i.e., suitable turbulence models), the ramps were designed based on intuitive arguments. The effects of the small ramps on the plume structure were significantly more pronounced than expected, and they were strongly dependent on the ramp geometry. For one particular ramp, the normally very strong counter rotating vortex pair (20,000-30,000 /s) was reduced in strength to the point of being undetectable with laser based Mie scattering experimental apparatus. On the other hand, a second ramp configuration produced stronger vortices within the plume. The aforementioned

18

lack of understanding of the flow physics made determining the physical mechanisms responsible for the effects of the ramps on the plume structure unattainable. However, the recent simulations of Chenault, Beran and Bowersox (1999) indicated that the recompression shock is a main vorticity production mechanism. Hence, the most likely case for the plume vorticity control is that the ramps reshape the recompression shock. Once these flow processes are better understood, methodologies that range from simple fixed ramps to sophisticated nonlinear adaptive control using micro-electrical-mechanical systems (MEMS) can be developed to control the jet plume features (e.g., shape, trajectory and unsteady, three-dimensional nonlinearities). Thus, optimizing the performance of numerous engineering endeavors.

Chapter 3

New Facilities and Apparatus Development

As was indicated in Chapter 1, the first phase of this research program entailed developing a hypersonic experimental research laboratory. This section provides a detailed description of the facility and apparatus development work that was accomplished in the research program.

3.1 Wind Tunnels

3.1.1 Mach 5.0 Wind Tunnel

Originally, it was proposed to convert the Mach 5.0 nozzle, test section and diffuser into a Ludwieg Tube facility with a refractive heater. However, additional funding from an alternate source became available and a high-pressure (306 atm) compressor was purchased. Hence, the facility was redesigned as a Mach 5.0 blow-down tunnel with a 6.0 second run time, which corresponds to a 4.7 km long stream tube. The free stream Mach number was measured as 4.9 with a ±2% variation across the test section core flow. The operating conditions are listed in Table 1.1. A schematic of the wind tunnel, along with a photograph, is given in Fig. 3.1.

20

The high-pressure air supply pumping system was a Hypres Air System Model HP-6000-NA4-E3 four-stage, reciprocating air-cooled air compressor, which was driven by a 7.46 kW (10 hp), 230 VAC Marathon Electric motor. This system provides a flow rate of 5.66 liter/s (12 cfm). The air from the compressor was cooled and dried by inerstage coolers and separators, and purifier desiccant cartridges. The system provided grade E breathing air [CO < 10 ppm v/v, CO_2 < 500 ppm v/v, total hydrocarbon content < 25 ppm v/v, oil (condensable mist/vapor) < 5 ppm w/v] with a dew point of -45 °C [63 ppm v/v (0.05 mg/l)]. The 30 MPa (4400 psia) high-pressure air was stored in eight DOT air bottles, each with a volume of 0.058 m^3. The time to compress from atmospheric to full capacity was approximately four hours, and a full supply of air was sufficient for nominally four wind tunnel runs. A second Hypres Brand HP-6000-NA3-E3 three-stage compressor system was purchased. This three-stage system is very similar to the above-described four-stage system. The system, which driven by a 5.59 kW (7.5 hp) motor provides an additional 4.25 liter/sec (9 cfm) grade E air.

Because the mass flow rate for the tunnel exceeded that available directly from the bottle farm, the air for single run was transferred to an intermediate tank for temporary storage and high volume blow-down. The intermediate tank consisted of three 6.0 m sections of 10.16 cm (4 inch) diameter schedule 120 stainless pipe. The tank volume was 0.11 m^3, and the intermediate pressure was set at 15.9 MPa (2,300 psia). The air from the intermediate tank flowed to the tunnel through a 2.54 cm (1.0 inch) stainless steel tube. Two Grove Model 302G Pressure Reducing regulators, located in series, regulated the pressure of the air entering the wind tunnel to within ±2% of the

desired pressure. The dome pressure for the first regulator was set at 5.86 MPa (850 psia) and the second was set 5.17 MPa (750 psi). These settings overcame the pressure drop in the system (plumbing and pebble bed heater) to provide a total pressure at the nozzle of 2.34 MPa (340 psi).

To prevent oxygen liquefaction, a pebble bed was designed to heat the air before entering the nozzle. The pebble bed heating system was designed and constructed in-house for this project. A rectangular (interior dimensions of 12.7 x 12.7 x 49.53 cm^3) high temperature grade stainless steel (RA321) vessel held the pebble bed. The pressure vessel was constructed from 5.08 cm thick plates, and was pressure tested with hydraulic oil to 17.24 MPa (2500 psi). Shown in Fig. 3.2a is a photograph of the pebble bed. The pebble bed consisted of stainless steel (316) pebbles with diameter of 6.35mm each. The pebbles absorbed thermal energy when low-pressure heated air flowed through. Two preheat system were constructed to produce the high temperature bed.

The first system consisted of a Sylvania Brand model R6325A-10 blower [1.38 kW (1.85 hp), 61 m^3/min (200 cfm)] and an Ogden Brand model ACK5A ʋ469 electric air heater (25 kW). This system was designed to preheat the bed in approximately forty-five minutes. However, the low-power blower was unable to overcome the pressure drop in the heater and pebble bed. Thus, approximately 90% of the blower air was routed around the pebble bed. As a result, the heat-up time was nominally four hours. This system failed after the first seven hundred runs. Hence a new preheat system was designed and implemented. In this system, the air was heated with two Reheat Brand model PF0-12 all stainless electric air heaters (1.2 kW each). An Eagle Model C7180V1

reciprocating single stage compressor [5.4 kW (7.5 hp)] provided the low-pressure (0.2 MPa) air at a rate of 9.1 m³/min (30 cfm). An Arrow brand model RH203 heatless twin tower regenerative desiccant air dryer (-40° C), with micron particulate filters, was used to ensure that moisture and oil vapor did not accumulate on the pebbles during preheat. The preheat system required two-and-a-half hours to heat the pebble bed from room temperature to 367 K (200°F). The high-pressure air for a tunnel run obtained thermal energy via convection from the pebbles when passing through the pebble bed.

The Mach 5 contoured nozzle was 34.3 cm long with throat area of 1.93 cm². A photograph of the nozzle is presented in Fig. 3.3. The nozzle was designed by the PI and constructed in 1995 from a high temperature grade (type 347) stainless steel. The original flow straightner consisted of a single aerogrid (i.e., porous plate) with forty 6.35 mm diameter holes located approximately 3.8 cm upstream of the nozzle contraction. The Mach number was uniform to within 2.0% across the free stream. However, the Mach number in the boundary layer varied significantly in the span wise direction. Because of this variation, a new flow straightner was designed and constructed. The new straightner consisted of two aerogrids each with sixty 3.2 mm holes located 2.54 cm upstream of a new turbulence-dampening screen. Figure 3.4a shows the new flow straightner and the original aerogrid. The new straightner was constructed from a high temperature grade (type RA321) stainless steel. The screen was located approximately 5.1 cm upstream of the nozzle contraction. It is also noteworthy that the stilling-chamber-to-throat contraction area ratio for increased from 13:1 to 19.4:1 with the new straightner. Presented in Figs. 3.4b and c is a comparison of the flow before and after the

new flow straightner measured with the Pitot tube in the five-hole-probe. The boundary layer with the new straightner is significantly more uniform across the span of the flow. However, the free stream was only modestly improved.

The stilling chamber Pitot pressure was measured with a 0-3.4 MPa gage Endevco Brand Model 8510B-500 piezoresistive pressure transducer with sensitivity 8.44 mvolt/pa. The miniature pressure transducer (3.8 mm face diameter) had a resonance frequency of 500 kHz and stable operation over a temperature range of 0-366 K. It was connected to a 2.38 mm outer diameter stainless tube, which was inserted into the chamber and mounted to the nozzle sidewall by a high-temperature resistant epoxy seal. The transducer was connected to an Endevco Model 4428A Pressure Indicator with LED pressure display and a 0 - 5volt analog output. An Omega Brand K-type (Chromel-Alumel, 3.15 - 1445 K) thermocouple connected to an Omega Brand Model DP25-TC-A programmable digital thermocouple meter displayed the tunnel chamber total temperature and provided a 0 - 10 volt analog output, with a scale factor of 283.15K/volt. The uncertainties in the total pressure and temperature were ± 0.02 MPa and ± 2 K, respectively.

The test section had a 7.62 × 7.62 cm^2 cross-section, with a length of 26.7 cm. The test section sidewalls were constructed from type 347 stainless steel and had optical grade glass windows (flat to within 52 nm/cm) for optical measurements. One of the top walls had three slots with corresponding blocks for probe insertion at different axial positions, and the other was a solid plate manufactured from 4.45 cm thick optical grade Plexiglass for optical access. The wind tunnel models (Figs. 1.1 and 1.2) were located in

the lower wall. The leading edge of the diamond injectors was located 7.14 cm downstream of the nozzle exit. Shown in Fig. 3.5 is the test section geometry.

The variable area diffuser was 7.62cm wide and 91 cm long. The throat-area was adjusted to 7.6 cm (28.3 cm downstream of the diffuser inlet), for optimal diffuser efficiency. The minimum pressure ratio was measured at 21, which corresponds to a diffuser efficiency of approximately 75%. Considering the compact size of the diffuser, this efficiency was deemed acceptable. The tunnel air discharged to the atmosphere through an Allied Witan Co. model M60 air sound muffler, which was attached to the diffuser exit through a 15.24 cm (6 inch) pipe.

3.1.2 Mach 7.0 Shock Tunnel

A reflective mode, true flight enthalpy Mach 5.0 or 7.0 shock tunnel was designed. Construction has begun and the tunnel is nearly completed. Figure 3.6 shows the shock tunnel schematic along with photographs of the existing hardware.

The driver tube was constructed from high-pressure 10.16 cm (4 inch) diameter stainless steel pipe. The pressure rating was 220 atm (3200 psi). The Air Force Research Laboratory through a separate Educational Partnership Agreement provided the pipe for the driver tube. The driver tube is 6.0 m (20 ft) long. The driven tube was constructed from five 6.0 m sections of 10.16 cm (4 inch) diameter stainless steel pipe. The pressure rating for driven tube is 61 atm (900 psi). The shock tube stands were constructed and the flanges were welded to the pipe in-house. The primary diaphragm holder, to be

placed between the driver and driven tubes, was designed, and construction has begun. Once the diaphragm holder is constructed, tests will be performed to document the tube recoil and acceleration loads. With this data, the secondary diaphragm holder, to be placed between the driven tube and the nozzle with a 90-degree turn, will be designed. This holder will require an in-house designed slip joint so that the nozzle and test section will not be subjected to the primary diaphragm rupture loads.

Two relatively large-scale, axisymmetric, contoured nozzles (Mach 5 and 7) were provided by Boeing. The exit diameter of each nozzle was 32.4 cm (12.8 inch). The test section design has not been finalized. However, a preliminary design study has been performed and costs were estimated for the follow-on grant. The last facility item is the vacuum receiver tank, which was purchased and tested. It is anticipated that the shock tunnel construction will be completed this year.

3.1.3 Low Reynolds Number Calibration Wind Tunnel

The cross-film probes are sensitive to Reynolds number. Hence, the probes had to be calibrated over the range expected across the injector plumes. Thus, a low Reynolds number calibration in-draft facility was constructed. The facility consisted of a Mach 1.7 contoured nozzle connected to the shock tunnel vacuum receiver tank. The cross-section of the calibration facility was 7.62 x 7.62 cm^2. Shown in Fig. 3.7 is a photograph of the calibration facility. The measured Mach number is 1.73, and the Reynolds number per meter is 14 x 10^6.

3.2 Wind Tunnel Models

3.2.1 Single-port-injectors

Four diamond injectors, with different incidence angles, and one circular injector (90°) were designed, constructed and tested. Figure 3.8 shows the injector schematics. The effective diameter of all injectors was 4.89 mm. The ducts for the diamond-shaped injectors were machined to angles of 10°, 27.5°, 45°, and 90° respectively with respect to the surface of the injector exit port. A 135° injection was achieved by operating the 45° injector backwards. All of the single port diamond injectors had a 15° vertex half angle. This small angle was chosen to ensure attached shock waves near the wall and to minimize the effects by the reflected waves from the side-walls. The injector was mounted on the bottom plate of the test section as shown in Figure 3.5. The injectant air was induced into the wind tunnel model through an aluminum duct with a diameter of 1.27 cm. The jet exit Mach number was 1.0. The jet-to-free stream momentum flux ratio (J) was varied by varying the injector total pressure. The jet flow conditions are listed in Table 1.2.

The tapered ramp of Wilson, Bowersox and Glawe (1998) was chosen to enhance the plume vorticity, where in the Wilson et al. study, this ramp produced the largest gain in plume vorticity. The 45° diamond injector was chosen as the test bed for the variable wall geometry ramp. This ramp was designed such that the ramp angle matched that of the injector (45°) and the height was chosen so that the vertex of the ramp was adjacent to

27

the lower side of the plume. These measures were taken to ensure strong ramp-plume interaction, while not overwhelmingly distorting the flow with the ramp. Figure 3.9 shows the final ramp geometry.

3.2.2 Distributed-Array-Injector

The distributed-array-injector was designed and constructed. For ease of manufacture, a 45° inclination angle was chosen. The spacing was chosen so that at higher momentum ratios, the adjacent plume interaction was incipient. This was desirable to maximize the isotach curvature. Therefore, the lateral separation was $2.5d_d$. The axial separation was $10d_d$. Thus, the plate consisted of eight inline rows of eight injectors. The injectors were diamond shaped with a 20° half angle. The larger half angle was chosen to ease the manufacture of the sixty-four small jets. The effective diameter for each jet was 2.2 mm. Presented in Fig. 3.10 are a schematic of the injector layout and the injector geometry.

The plate was manufactured as a laminate. A special machine tool was purchased with a 140° tip. The tool was then used to machine half diamond groves (1.15 mm deep at the vertex) across the 5.0 mm laminate. The laminates were then fascined to form the eight rows of eight diamond injectors.

3.3 Computational Facilities

The majority of the three dimensional calculations took place on the University of Alabama System Cray supercomputer, which came on-line with the new SV1 processors in August of 1999. The Cray SV1 system is a parallel vector processing supercomputer with a tightly coupled I/O system. It contains 16 CPUs, 2048 million-words of central memory and 480 gigabytes of RAID-3 fibre channel disk storage. The SV1 interfaces to the statewide network through a fiber distributed data interface (FDDI) ring located at the Alabama Supercomputer Center (ASC). The sixteen CPUs are homogenous and can process in scalar and vector mode. Groups of four SV1 processors can be configured as multi-streaming processors (MSPs). An MSP has a peak processing rate of 4.8 GigaFLOPS. The clock period is 10.0 nanoseconds; the cycle time is 4 FLOPS/clock cycle; the vector units are 32 per processor; the address space is 2048 million words; the maximum bandwidth/channel is 6.4 GB/second, and the maximum result rate is 1.2 GigaFLOPS. In addition, the department and college of engineering maintain numerous SGI, IBM and DEC workstation laboratories for data processing.

3.4 Instrumentation

3.4.1 Surface Oil Flow Visualization

Dow Corning Brand 200 fluid (Dimethicon) with a kinematic viscosity of 1000

centistokes, which is a medium viscosity linear polydimethylsiloxane polymer, was used for surface oil flow visualization. Day-Glo Color T-15 blaze orange fluorescent pigment was mixed with the fluid. The mixture was spread on the bottom surface of the test section and illuminated by an ultraviolet lamp through the top surface of the wind tunnel, which was constructed from optical grade Plexiglass. Photographs of the oil patterns were taken with a Kodak Professional DCS 460c color digital camera that was mounted on a tripod above the top plate. The Kodak camera back, which was attached to a Nikon N90 camera body, had a high-resolution 3060x2036 pixel color Charge Coupled Device (CCD) imager. A Nikon N90 50 mm lens was used, and the shutter speed and f-stop were 1.3 and 2.8, respectively. The camera was connected by a SCSI port and cable to a NEC personal computer with a 300 MHz Intel Pentium 2 processor, 64MB Sync DRAM, 8.4GB hard drive PC that operated with Microsoft Windows 98. On the computer, an Adaptec AVA-1502 SCSI Host Adapter with a SCSI2 port transferred the digital images recorded by CCD imager to the computer, where the images were acquired and displayed through the Kodak TWAIN driver into the Adobe Photoshop 4.0 application software for Windows. The image recording was controlled via the Adobe Photoshop program.

3.4.2 Two-Color Digital Particle Image Velocimetry (PIV)

The laser sources used for the present PIV measurements were two Continuum Brand Surelite SL I-10 Nd: NAG laser systems. The two Surelite Nd:NAG lasers each produced coherent green (532 nm) laser beams. The red (607 nm) laser beam was

30

formed by passing one green beam through a SulfaRhodamine (640 nm) methyl alcohol solution dye laser. The two (green and red) laser beams were then merged in space through a dichroic splitter, and the resulting co-located beams were passed through sheet-forming optics and directed into the test section. The temporal delay between the red and green laser was set at 200 ns with a Stanford Research Systems Model DG535 four-channel digital delay/pulse generator. The Kodak Model DCS 460 high resolution CCD camera (described in the previous Section) with Nikon N90 50mm and 150 mm lenses were used to record the Mie scattering color images.

A TSI Brand Model 9306 Six-Jet Atomizer was used to produce olive oil seed particles with mean aerodynamic diameter $\leq 0.6\mu m$. The particles were injected with the injector air. Because of the high pressures associated with the Mach 5.0 wind tunnel, the seed generator was placed inside a pressure vessel.

Because of the high fidelity temporal laser separation control, the digital two-color system was well suited for hypersonic flow. The PIV system provided direct measurements of the instantaneous planar velocity (in the x and y directions) and vorticity. In addition, the instantaneous Mie scatter images provided qualitative insight into the large-scale turbulent structure of the flow. Unfortunately, this PIV system was not robust enough to acquire enough images for statistical turbulence measurements. More specifically, the camera acquisition rate translated into one PIV image per tunnel run. Hence, only instantaneous information was obtained.

3.4.3 Pressure Sensitive Paint (PSP)

Pressure sensitive paint (PSP) provides surface pressure distributions with larger areas and finer spatial resolution than conventional pressure ports. The ISS, Inc. Brand platinum octaethylporphyrin (PtOEP) pressure sensitive paint was used to measure the surface pressure distribution around the jet port. It had absorption maxima at excitation wavelengths of 380 and 540 nm, with an emission at 650 nm. Because the present pressure sensitive paint utilized fluorescence, a relatively high frequency response ($\sim$ 1 msec) was achieved. The intensity of the imaged surface is governed by the Stern-Volmer relation (i.e., $I_o/I = 1 + cp/p_o$), where c is constant that depends on the molecular properties of the paint. The actual calibration was slightly more general (i.e., $I_o/I = a + bp/p_o$).

The paint, when excited with a blue LED light source, produced photoluminescence in order to lose the absorbed energy, and some of the photoluminescence was quenched by the local oxygen (a pressure dependent parameter). Hence, the luminescence intensity was pressure dependent. The luminescence intensity generated by the coating was then collected by the Pixelvision SpectraVideo Brand CCD back-illuminated gray-scale camera, model SV512V1A/PFT-95 with a Nikon f/16-50 mm lens. Uncertainty estimates are listed in Table 3.1.

3.4.4 Traverse and Linear Voltage Displacement Transducer

The traverse system consisted of a 15W Bodine Electric Model NSH-12 DC fractional horsepower gear motor that drove a slide, which moved the probe up and down in the y-direction. The traverse speed was controlled by a Minarik Electric Model SL15 controller. The speed was set as 7.62 mm/s (at 70% of full power). The start and stop of the traverse was controlled by a Magnecraft Electric W211ACPSOX-5 delay on start relay and a Magnecraft Electric W211ACPSRX-5 delay on ending relay, respectively. To obtain measurements during the steady flow period, the traverse system was delayed two seconds after the tunnel start, and stopped to end traverse measurement after five seconds.

The position of the probe was recorded by an Omega Model LD100-150 Linear Voltage Displacement Transducer (LVDT) with nominal linear range 152.4 mm. The LVDT is a precision variable inductor with frequency response up to 15 kHz. An Omega Model SP200A signal processor received signals from LVDT, and generated a DC voltage proportional to the inductance, which was linear with core displacement. The uncertainty of LVDT measurement was 0.067 mm.

3.4.5 Five-Hole Pressure Probe

An Aeroprobe Inc. Brand five-hole-probe was used to measure the local mean Mach number, Pitot pressure, static pressure and total pressure. The probe was a 19°

semi vertex angle axisymmetric cone constructed from stainless steel, with a blunted tip containing the Pitot probe. There were four elliptical shaped pressure taps, formed from 0.79 mm outer diameter tube, at a 90° interval around the circumference of the cone. The cone tip was soldiered to an L-shaped 1.59mm outer diameter stainless tube, which held five 0.79 mm outer diameter miniature stainless tubes. The space between the tubes was filled with steel wire and epoxy to prevent displacement. The L shape tube was inserted into a 6.35mm thick and 14.6cm long stainless streamlined strut with sharp leading and trailing edges. The five taps, which were connected to the five 0.79 mm outer diameter miniature stainless tubes, were connected to the pressure transducers through five 1.59 mm outer diameter miniature Tygon R-3603 tubes. The Pitot pressure was measured an Omega 0-0.69 MPa (0-100 psia) Px139-100A4V pressure transducer, and the four static pressures were measured with four Omega 0-0.10 MPa (0-15 psia) Px139-15A4V transducers. All five transducers were excited with an Omega PSS-5A power supply. Each transducer had an output 0.25-4.25volts and a 4.8mm outer diameter inlet connector. Based on the normal shock and Taylor-MacColl conical flow theory, the Mach number is a unique function of the ratio of the cone-static and Pitot pressures. The numerical conical flow and Rayleigh Pitot solution is tabulated Table 3.2. A curve fit for the Mach number as a function of the pressure ratio is given by

$$
\frac{1}{M} = -1.424 + 24.873\left(\frac{P_c}{P_{t2}}\right) - 158.089\left(\frac{P_c}{P_{t2}}\right)^2 + 566.284\left(\frac{P_c}{P_{t2}}\right)^3
$$
$$
-1124.770\left(\frac{P_c}{P_{t2}}\right)^4 + 1165.510\left(\frac{P_c}{P_{t2}}\right)^5 - 491.796\left(\frac{P_c}{P_{t2}}\right)^6
$$

The percentage differences between the curve fit and the exact theory are also listed in Table 3.2. A comparison of the calibration curve fit to the numerical solution is given in Fig. 3.11. The remaining flow properties were computed using the usual compressible flow relationships [Anderson (1990)]. An important inference from Fig. 3.11 is that at high Mach numbers, greater than 5.0, the change in Mach number becomes very sensitive to small changes in the pressure ratio; this is because of hypersonic similarity. Hence, the uncertainties in the Mach number are amplified at higher Mach numbers. The uncertainty estimates for the Mach number and static pressure acquired with this probe listed in Table 3.1 are given as a function of Mach number. It is also noteworthy that the present study was focused on the plume and boundary layer regions of the flow (M < 5), and thus, the hypersonic similarity difficulty was avoided.

3.4.6 Hot-Wire Anemometry System

The Hot-Wire Anemometry data was taken using an IFA 300 Constant Temperature Anemometer System manufactured by TSI Incorporated. The system consisted of an IFA 300 anemometer cabinet with two channels and a 16 channel A/D board. The IFA 300 provided an analog output in the range of -5 to 5 volts. TSI model 1243-20 (x-y) and 1243-20AN (x-z) cross-film probes were used. Cross-film probes were used instead of cross-wire probes because the films were more rugged and survived longer in the harsh Mach 5.0 environment. The cylindrical hot-film sensors were very

similar in appearance to the wire sensor, but with a larger diameter and a slower frequency response (~ 150 kHz). This tradeoff was deemed appropriate for this research. The cross-film probe data were collected using the data acquisition system described below at a sampling rate of 100 kHz per channel. In order to record the height of the hot film probes in the boundary layer, the LVDT and linear traverse combination described above was used.

Bowersox (1996a,b) presents a detailed development of the cross-wire response. The data analysis extends the normal-wire methods of Kovasznay (1950) and Spangenburg (1955) to the cross-wire probe. A FORTRAN program, MSHEAR v. 1.0, was developed by the PI to perform the multiple overheat cross-wire data reduction. WinMSHEAR v. 1.0 uses the MSHEAR routines in a windows environment. For the multiple overheat analysis, six to eight wire temperatures per probe were used.

Multiple overheat cross-wire anemometry provides the mean mass flux, $\overline{\rho u_i}$, the mean total temperature, $\overline{T_t}$, the mass flux components and total temperature fluctuation turbulence intensities, $\sqrt{\overline{(\rho u_i)'^2}}$ and $\sqrt{\overline{T_t'^2}}$, and the $\overline{(\rho u_i)'(\rho u_j)'}$, $\overline{(\rho u_i)'T_t'}$ correlations. The compressible Reynolds shear stress is related to the cross-wire turbulence data as follows [Bowersox (1996b)]

$$\tau_{ij}^T = -\frac{\overline{(\rho u_i)'(\rho u_j)'}}{\overline{\rho}} + \overline{\rho u_i}\,\overline{u_j}\left(\frac{\rho'}{\overline{\rho}}\right)^2$$

where the first term on the right-hand side is directly measurable with the cross-wire. An

important attribute of this equation is that for thin layer type flows, where the transverse or span velocity is generally very small, the second term on the right-hand side is usually much smaller than the first, which was the case for the present work. Thus, direct measurement of the full compressible Reynolds turbulent shear stress was possible. Also, the Favre averaged turbulent heat flux is directly measurable with multiple overheat cross-wire anemometry. Uncertainty estimates are listed in Table 3.1.

In addition to the time averaged results, hot-wire probes were used for temporal correlations, spectral (FFT) analyses, and conditional sampling. In addition to frequency content, temporal autocorrelation functions, and the associated micro and integral length-scales, were obtained. Uncertainty estimates are listed in Table 3.1.

3.4.7 Data Acquisition Boards and Testpoint Software

The analog signals from the various probes (except the cross-film, discussed in the next paragraph) were converted to digital signals with a 12-bit resolution, Keithley Model DAS-1802AO low-gain data acquisition board. This system could acquire data at a rate up to 333 ksamples/s, with a maximum A/D throughput of 312.5 ksamples/s for operation in the 0-5volt unipolar mode. All channel inputs were within a range of 0-5 volt in order to increase total system throughput and reduce noise by using the same gain for all channels. The system is software-configurable for sixteen single-ended onboard channels or eight differential channels. The data board, with the STA-1800U screw terminal I/O interface accessory, was connected to an IBM Pentium(r) OverDrive 56MB

RAM PC operating Windows 98. The Capital Equipment, Inc. data acquisition control software package Testpoint was used to control the data acquisition. The total number of samples and sampling frequency were 10,000 and 1 kHz, respectively. Consequently, the data-taking period was 10 seconds.

The cross-film voltage data was recorded using a data acquisition system that was integrated with the TSI IFA 300 Anemometer. The data acquisition system consisted of an Analog to Digital (A/D) conversion card, and a Gateway 100 MHz Pentium personal computer. The A/D board used was a model ADCWIN-16 board provided by TSI Incorporated and consisted of 16 channels with a maximum sampling rate of 500 kHz. The hot-film data were recorded at a rate of 100 kHz per channel using the data acquisition system in combination with the aforementioned IFA 300 system and the acquisition software provided by TSI Inc.

3.5 Numerical Navier-Stokes Solvers

3.5.1 GASP

The AeroSoft, Inc. numerical Navier-Stokes program GASP was used for the initial flow field simulations. GASP is AeroSoft's structured, multi-block, finite volume flow solver which is applicable to compressible flow fields approximately Mach 0.2 and greater. A detailed description of GASP is given in the User's Manual (Aerosoft, Inc., 1999). Germane to the present research, GASP offers a relatively extensive list of

algebraic and two-equation turbulence models.

3.5.2 ISAAC

The NASA Langley research Navier-Stokes program ISAAC was used to evaluate second order transport turbulence modeling. ISAAC is a 3-D, finite volume structured flow solver. A complete description of ISAAC can be found in Morrison (1992). The primary benefit of ISAAC is that it includes the Zang, So, Gatski, and Speziale second order Reynolds transport turbulence model. Hence, ISAAC and GASP together provide a wide range of turbulence model capability.

Chapter 4

Jet-Interaction Flow Field Results

4.1 Single-port-injector

4.1.1 Flow Visualizations

Given in Fig. 4.1 are the flow visualization results. Focusing first on the surface

oil flow visualizations in Fig. 4.1a, and moving in the stream wise direction, the first flow

feature, just upstream of the diamond jet, is the leading edge jet-interaction-shock. As

can be seen in Fig. 4.1a, the jet-interaction-shock was attached to the diamond injector

for the 10, 27.5 and 45° injectors. The 90° injector generated a detached bow shock. The

second feature is the horseshoe vortex that wraps around each side of the injector. The

third noticeable characteristic is the trailing edge shocks (recompression shocks), which

were nearly planar. Shown in Fig. 4.1(b) are the 135° and 90°-circular injector surface

oil flow visualizations. The main difference in the surface oil flow pattern is the shape

and strength of the jet-interaction-shock. For the 135° injector, the jet-interaction-shock

is very nearly planar and normal to the flow, which results in a large total pressure loss,

although, not as extreme, a similar conclusion holds for the 90°-circular injector.

The surface oil flow visualizations also provided quantitative information, which

is relative to injector design. The data from the subsequent analyses are summarized in Table 4.1. The first column in Table 4.1 shows the Mach number, M_l, estimated from shock expansion theory based on the measured shock angle and the 15° diamond orifice. The effective back-pressure is defined as the pressure to which the jet will expand [Fuller et al. (1992)]. For normal injection through a circular orifice, the effective back-pressure has been modeled as approximately $0.8p_2$, where p_2 is the pressure downstream of the normal shock. For angled injection, the effective back-pressure has been modeled as the surface pressure on a cone at the injection angle. For the present diamond orifices, the effective back-pressure, p_{eff}, was calculated, using shock-expansion theory based on M_l, as the average pressure around the circumference of the diamond orifice. Effective back pressure estimates from the surface oil flow were not possible for the detached shock cases. However, the effective back-pressure is further discussed (below) with respect to the pressure sensitive paint measurements.

For the attached shock cases, the jet-interaction-shock shape was approximately planar. One line of the plane, along the tunnel floor was measured from the surface oil flow, and since the shock was attached to the jet, a second line in the plane was along the jet flow leading edge. With these two lines, the planar shock was defined and the normal component of the free stream Mach number was computed. The total pressure loss through the diamond shaped shocks was estimated with the normal component of the Mach number. A normal shock was assumed for the cases with detached shocks. The total pressure loss translates directly into drag, and the data show that shock losses decrease significantly (loss of 10% for the 10° injector to over 93% for the detached

41

shock cases) with decreasing injection angle; this was the expected result.

Mie-scattering flow visualizations for the diamond injectors (J = 0.43 and α = 10, 27.5, 45 and 90°) are also shown in Fig. 4.1a. These data provide additional penetration information, and the entrainment effectiveness can be gleaned from the size of the large-scale structures, where it was presumed that the larger structures entrain larger amounts of the free stream. Hence, the entrainment (i.e., large-scale structure) size was observed to increase with increasing injector incidence angle. Originally, it was anticipated that the particle image velocimetry would provide high-resolution turbulence data. However, only one image per wind tunnel run was accomplished with the present system (described in Chapter 3). Hence, only instantaneous velocity vectors for each of the four injectors were obtained. Because these results did not contribute to the flow field understanding, they were not discussed here.

4.1.2 Five-Hole-Probe

Shown in Fig. 4.2 and 4.3 are the Mach number and Pitot pressure contours at *x/d* = 5.0, *J* = 0.47 for the 10-90° diamond injectors and the 90°-circular injector, respectively. This location was chosen as the most upstream location because, based on the Mie-scattering images, the flow angles across the plume for all cases were relatively small -- this was mainly to assure probe accuracy. A number of features are noticeable on the contours. These features become more prominent at the higher injection angles. Because of the more prominent characteristics, the present discussion will focus first on

the 90° injectors (Figs. 4.2d and e), however the subsequent discussions are relevant to all of the cases.

At first glance, the plume appears to be the low Mach semicircular region (blue) centered at $z/d = 0$. However, this wake region is the result of the plume engulfing low momentum boundary layer fluid, and the plume extends further into the flow. The outer edges of the plume are difficult to discern because the relatively thick ($\delta/d \approx 2.5$) incoming hypersonic boundary layer. Comparing the Mie scattering images and the Mach counters indicated that the upper most point in the plume was located at the point along the z-axis where the Mach number reached a value of approximately 5.0. Qualitative estimates of the plume penetration (y_{max}) using this criterion and cross-sectional area ($A_p \approx \pi y_{max}^2$) were obtained from the data in Figs. 4.2. The results are summarized in Table 4.2. As expected, for a given momentum ratio, the size and penetration of the plume increased with increasing injection angle. The facility boundary layers are also clearly depicted on both sides of the plume. The familiar boundary layer thinning [McCann and Bowersox (1996)] in the areas adjacent to the plume were observed here. Around the periphery of the plume is narrow area of inviscid flow. Narrow shock layers like the ones noticed here are defining characteristics of hypersonic flow [Anderson (1990)]. The maximum Mach number in this region exceeded the free stream value, where the peaks were nominally 6.0. This over expansion to a Mach number higher than the free stream is consistent with the 2-D supersonic results of Bowersox, Tucker and Whitcomb (2000), where the plume turned slightly down toward the wall, and caused a second weak recompression shock. McCann and Bowersox

43

(1996) also observed higher Mach numbers around the periphery of the plume. The arching structure above the inviscid region is the jet-interaction-shock. For the diamond injectors, the shock shape echoed the diamond shape.

The Mach contour and Pitot pressure distributions at $x/d = 21$ are shown in Fig. 4.4 and 4.5. The test matrix was expanded at this station and covers all of the test conditions listed in Table 1.2, where the last two test conditions (i.e., with vorticity control ramps) are discussed in Section 4.4. The defining characteristics for the no-ramp cases at this station are similar to the one described above. Hence, that discussion will not be repeated here. Qualitative estimates of the plume penetration and cross-sectional area were obtained from the data in Figs. 4.4, where again M = 5.0 was used as the criteria. The results are summarized in Table 4.2. Again, for a given momentum ratio, the size and penetration of the plume increased with increasing injection angle, and for a given injector angle, the plume penetration increased with increasing momentum ratio.

Also, noticeably absent from all of the diamond injector contours is the familiar counter rotating vortex pair induced cardioidal plume shape. Referring to the circular injector, Fig. 4.2e, the two "dog-ear" features located near $y/d = 1.5$ and $z/d = \pm 1.2$ are clear indicators of a relatively strong, compared to the diamond injectors, vortex pair. However, the levels appear to be much lower than the supersonic results of McCann and Bowersox (1996). Two factors were deemed important towards producing this effect. First, the recompression shocks for the diamond injectors were planar, as compared to the curved shocks for the circular injector. Hence, either Crocco's anisentropic term or the baroclinic torque vorticity production mechanisms (or both) were reduced as a result of

the planar shock. Second, the hypersonic free stream possessed a very high momentum, as compared to the injection flow, and the incoming hypersonic boundary layer was relatively thick ($\delta/d \approx 2.5$). Therefore, the plumes did not push far out into the free stream. Thus, the large pressure gradient and high circumferential shearing levels (discussed in Chapter 2), which contributed to the plume vorticity, were both reduced. The present reduced plume vorticity has important implications with respect to predictions. Specifically, one of the key limitations in prediction accuracy is the poor modeling of the effects of highly three-dimensional flow on the turbulent transport. It appears from the present measurements, that the flow field for hypersonic injection with thick boundary layers may be experience weaker extra three-dimensional strain rates, and thus more accurate numerical simulations. Our cross-wire measurements (currently in-progress) will provide definitive measurements of the plume vorticity.

4.1.3 Pressure Sensitive Paint

The pressure sensitive paint results are shown in Fig. 4.6, where the flow is from the bottom to the top. The red diamonds located near the bottom of the first four images denotes the injectors. The uncertainty for the measurements was estimated at ±0.15 psi, which for the 10° injector is on the same order of magnitude as the pressure variation created by the jet. However, the flow features are discernible for this case, and the data resolution improves with increasing incidence angle. Qualitatively, the surface pressure contours echo the surface oil flow features described above. However, in addition to the

shock waves, expansion fans are noticeable on the side corners of the injectors as the flow wraps around the jet. The pressure distributions for the 10° - 45° diamond injectors show the attached shock, and as expected the magnitude of the pressure variation increased with increasing injector angle.

The 90° diamond injector results again confirm the detached shock wave. The jump in pressure across the bow shock (i.e., p_2/p_1) was estimated as approximately 2.5, which indicated that $M_1 = 1.5$. The normal shock model (i.e., $p_{eff} = 0.8p_2$) for the effective back-pressure results in a ratio (p_{eff}/p_1) of 2.0, which is higher than the estimated value from the pressure sensitive paint, which was computed as the average around the periphery of the injector. The results are summarized on Table 4.1. The pressure sensitive paint results compare well with the estimates based on the shock-expansion calculations from the surface oil flow. In addition, the value from the numerical prediction for the 90° diamond injector (discussed in Section 4.3) also compares well with the pressure sensitive paint result.

Focusing now on the 90° circular injector, the injector exit is denoted by the dark red circle near the bottom center of the image. As expected, a high-pressure region is noticeable between the shock and the injector exit. As was the case for the 90° diamond injector, the pressure increased by a factor of approximately 2.5, which indicates that the Mach number (M_1 as listed in Table 4.1) just ahead of the shock is approximately 1.5. The pressure just downstream of the injector was approximately 30% of the free stream pressure. The effective back-pressure is also listed in Table 4.1.

4.1.4 Flow Field Description of Single-Port Injector with Attached Jet-interaction-Shock

The data in Figs. 4.1-4.6, with the results discussed in Chapter 2, allow for a reasonably complete description of the flow field. Presented in Fig. 4.7 is a schematic of the flow field with the salient features annotated. Note, the plume vorticity is shown, but the above data suggest that the levels are low. Detailed cross-wire measurements are in-progress that will provide direct measurement of the vorticity levels.

The current data also provide the basis for focusing the next step in this research project (to be completed as part of the follow-on grant). Specifically, the turbulent shear stress transport port equation is given by

$$\tau_{ij,t}^T + (\overline{u}_j \tau_{ij}^T)_{,j} = -\tau_{ik}^T \overline{u}_{j,k} - \tau_{jk}^T \overline{u}_{i,k} + \overline{u_j''}\overline{p}_{,i} + \overline{u_i''}\overline{p}_{,j} - \overline{\tau}_{ik,k}\overline{u_j''} - \overline{\tau}_{jk,k}\overline{u_i''}$$
$$-\overline{p'(u_{i,j}'' + u_{j,i}'')} - [\overline{(\rho u_i'' u_j'' u_k'')} - \overline{p'u_i''}\delta_{jk} - \overline{p'u_j''}\delta_{ik} + \overline{(\tau_{ik}'u_j'' + \tau_{jk}'u_i'')}]_{,k} + \overline{\tau_{ik}'u_{j,k}''} + \overline{\tau_{jk}'u_{i,k}''}$$

The right-hand-side consists of an unsteady term and the convection. On the left-hand-side, the first two terms are the production, the third and fourth terms are the pressure work, the fifth and sixth terms are the viscous work, the seventh term is the pressure-strain redistribution, the eight term, in brackets, is the diffusion, and the last term represents dissipation. The next step in the experimental program is focused on the direct measurement of the production terms associated with the additional strain-rates (vorticity) with cross-wire anemometry. The turbulence measurements will focus on the 45°, 90° and 90° circular injectors to quantify (1) the differences between the attached shock and detached shock diamond injectors and (2) the differences between the diamond

47

(planar recompression shock) and circular injector (curved recompression shock) cases.

4.2 Distributed-Array-Injector

4.2.1 Flow Visualizations

Testing of the distributed-array model was also performed. A surface oil flow visualization and color schlieren photograph are presented in Fig. 4.8. The surface oil flow shows that each jet produced a flow structure similar to that of the single-port-injector (Fig. 4.1). The flow field for the last row was however very distorted, which may indicate flow separation. In addition, the oil flowed downstream during the run, and hence, a relatively large amount had accumulated in this region, thus contributing to the distorted flow visualization.

The interaction shocks were attached for all of the injectors in the first seven rows, which was a design goal. The multiple rows of jet-interaction-shocks are clearly depicted in the schlieren. Although these shocks appear strong on the photograph, it is however important to note that the visualization is an integration of all eight injectors across the span. The shock angle in the free stream was measured as 15°, which is close to the Mach wave angle for Mach 4.9 of 12°. Hence, the shocks are relatively weak; considering a 2-D wave (worst case scenario), the total pressure loss would be less than 2%.

Detailed five-hole-probe measurements (Fig. 4.9) were obtained midway between

the 6th and 7th rows (i.e., 1.27 cm downstream of the trailing edge of row six.) The data were taken in 1.58 mm increments spanning the center ±6.35 mm in the z-direction. The data covered the center two span wise rows of jets so that the periodicity of the flow could be established. The arrows along the bottom axis in Figs. 4.9a and b show the locations of the two rows of jets. The Mach and Pitot pressure contours are symmetric about $z/d = 0$ (the single-port value for d was used for nondimensionalization here). The boundary layer edge for the undisturbed flow would have been at $y/d \approx 3$-4. The striations above this level are the result of the numerous shocks created by the multiple axial rows of jets. Below this level, the boundary layer region shows a strong corner structure near $y/d = 2$, $z/d = 0$, and the flow appears to be periodic in the z-direction about $z/d = 0$. This represents a curved line of constant Mach number, which translates into a curved isotach. This curved isotach was the desired result to produce corner flow vorticity (see Fig. 1.2).

The data in Figs. 4.8 and 4.9 indicated that the distributed-array-injector generated the desired flow field. However, the magnitude of the plume vorticity is suspect based on the single-port results discussed above. Vorticity production ramps, such as that discussed below in Section 4.4, may also be required. On-the-other-hand, the isotachs were curved, which is a vorticity production mechanism. Also, the distortions to the wall boundary layer were further away from the wall than desired. It is expected that fewer axial rows of smaller injectors at a lower incidence angle would be more affective by generating the desired flow lower in the boundary layer. More work is required to fully assess the viability of this method.

49

4.3 Preliminary Single-Port Computational Modeling

Preliminary numerical simulations of the flow field were obtained with the GASP code. The GASP code allows for grid sequencing to speed-up numerical convergence. For the present preliminary study, four levels [(33x9x17), (65x17x33), (129x33x65), (257x65x129)] are being used. It is not expected that grid converged solutions have been achieved at this point. Refined grid sequencing will be used to ensure grid convergence.

In summary, a thermally and calorically perfect gas was assumed. Roe's flux differencing was used. An upwind biased third order ϕ-κ scheme was used in the stream wise direction and second order central differences were used in the cross plane. The solutions were temporally converged such that the Euclidean norm of the numerical residual was reduced to a relative level of 1×10^{-3} or an absolute level of 1×10^{-6}.

Preliminary results for the Baldwin-Lomax turbulence model on the (257 x 69 x 129) grid are shown in Fig. 4.11. Overall, the Mach number contours, albeit on a different scale and not fully grid converged, show the same salient flow features obtained experimentally (Figs. 4.2d and 4.4d). The surface pressure distribution is also shown in Fig. 4.11. Again, the agreement with experimental data (Fig. 4.6) is considered very good considering the preliminary state of the simulations. The numerical effective back-pressure and plume penetration values are listed in Tables 4.1 and 4.2, respectively. The results are in reasonable agreement with the data. However, the plume size is over predicted by almost 30% at the downstream measurement station. Although, the results are preliminary, the low levels of vorticity across the plume seen

experimentally may contribute to the reasonably good agreement. Additional computational work is currently underway.

4.4 Single-Port Injector with the Vorticity Control Ramp

Presented in Fig. 4.12 are the Mach and Pitot pressure ratio across the plume of the 45° diamond injector with the tapered ramp (Fig. 3.9) present. Wilson, Bowersox and Glawe (1998) demonstrated that this geometry was very effective at increasing the plume vorticity. Thus, this ramp was chosen to increase the low levels of vorticity observed for the single-port cases described above. The goal here was to demonstrate that ramps are capable of imparting vorticity to the plume in a hypersonic flow with a thick boundary layer, which has numerous advantages for hypersonic boundary layer control.

Comparison of Fig. 4.12a with 4.4c (or Fig. 4.12b with 4.5c) demonstrated that the ramp had the desired impact on the plume structure. Specifically, with the ramp present. the plume penetration had increased by 13% and the plume shape was indicative of higher levels of vorticity, where the cardioidal shape was more pronounced. The larger more clearly defined plume indicates stronger vorticity and a higher level of entrainment. The penetration and plume size acquired from Fig. 4.12 are listed in Table 4.2. In summary, these results show that by varying the wall just downstream of the injector, the plume properties (penetration, size, vorticity, and entrainment) are controllable.

Chapter 5

Conclusions and Recommendations

5.1 Conclusions

The wind tunnel development effort was very successful. Two facilities were designed. Construction of the Mach 5.0 blow-down tunnel was completed and the tunnel has been run over eight hundred times for this project. This facility is relatively unique and offers a low-cost national wind tunnel resource for basic hypersonic flow research, and with the recent upgrades listed in Chapter 3, fifteen hundred runs per year are anticipated. The shock tunnel facility construction has proceeded at a good pace, and will be completed this year. This facility is also relatively unique, and will offer a large-scale high-energy hypersonic wind tunnel resource. A detailed description of each facility is given in Chapter 3 and the available flow conditions are listed in Table 1.1.

A new and extensive database for sonic injection into a hypersonic (M = 5.0) high Reynolds number (Re/m = 55 x 10^6) cross-flow was developed. To provide a broad database, injector configurations were tested. In addition, to provide complete flow field documentation, numerous experimental techniques (five-hole pressure probe, pressure sensitive paint, Mie scattering, color schlieren and surface oil flow visualizations) were employed. These data provided both insight into the overall flow structure and the basis to focus the follow-on turbulent measurement (cross-wire anemometry) effort. In addition, a distributed-array-injector was designed based on the single-port database, and

tested. Lastly, the use of variable wall geometry for plume vorticity control was tested. Detailed flow field descriptions for the various hypersonic jet-interactions were discerned (Chapter 4), and numerous flow field conclusions have been drawn. A brief listing is given below.

1. The jet-interaction-shock was attached to the jet leading edge for single-port injection through the diamond orifices when the incidence angles were less than or equal to 45°. Thus, producing reduced drag and eliminating potential hot spots, associated with the upstream flow separation, as compared to the cases where the shocks were detached.

2. The jet-interaction-shock induced total pressure loss increased with increasing injector angle. The loss increased by nearly a factor of ten over the range of single-port conditions tested.

3. The size of the large-scale turbulent structures, i.e., the entrainment, increased with increasing injector angle.

4. The plume penetration and cross-sectional area increased with incidence angle and momentum ratio.

5. The characteristic cardioidal plume shape that is indicative of the counter rotating vortex pair within the plume was absent from all of the single-port diamond injectors, and the circular injector results only showed modest levels of vorticity.

6. The distributed-array model was designed to be a low drag device that generates multiple "sheets" of axial vorticity. The results show that the design goal was

achieved. Although the plume vorticity level, as discussed in #5, may not have been as high as desired, the isotachs were curved and corner flow vorticity generation was expected.

7. A vorticity generation ramp was designed following Wilson, Bowersox and Glawe (1998). The ramp increased the penetration of the plume by 13%, and the plume shape was indicative of higher levels of vorticity.

8. The computational modeling accomplished to date is very preliminary, but the results shown here indicated that, as proposed, simple algebraic models have potential for this class of flows.

All of the observations listed above have direct application toward practical design of an injection scheme for hypersonic applications. However, the fifth observation also has theoretical implications toward control and prediction, and numerous factors were deemed important toward producing the apparent low levels of plume vorticity. First, the recompression shocks for the diamond injectors were planar, as compared to the highly curved shocks for the circular injector. Hence, either Crocco's anisentropic term or the baroclinic torque vorticity production mechanisms (or both) were reduced as a result of the planar shock. This result provides a potential method to directly control the plume vorticity. For example, the trailing edge of the injector port can be tailored or the wall downstream of the injector can be modified, as was tested in this work, to produce a specific recompression shock shape. Second, the hypersonic flow possessed both a very high free stream momentum, as compared to the injection flow,

and a relatively thick ($\delta/d \approx 2.5$) boundary layer. Therefore, the plumes did not push far out into the free stream. Thus, the large pressure gradient and high shearing levels (discussed in Chapter 2), which contributed to the plume vorticity, were both reduced. In terms of prediction, the lower levels of vorticity are desirable because current turbulence model are more appropriate. The follow-on cross-film measurements will provide direct quantification of the plume vorticity.

Two technology transfers have occurred because of this project. Specifically, the PI is working closely with the Air Force Research Laboratory to incorporate the diamond injector technology into current scramjet combustion development efforts, and the PI, as part of the follow-on research project, is examining, with strong interaction with NASA Langley, the use of diamond injectors for roll control of the X-43 flight test vehicle. In addition, the PI used the single-port database to design a distributed-array-injector plate for shock induced boundary layer separation control.

5.2 Recommendations

It is recommended that additional injector shapes (e.g., triangular and tear drop) be examined to better quantify the role of the recompression shock on the plume vorticity generation. In addition, the distributed-array model showed promise as a vortex sheet production device. However, the present effort was not sufficient to fully investigate the possibilities. For example, the reduced vorticity for the hypersonic injection was most likely more severe for the smaller injectors. Hence, downstream devices such as the

tapered ramp studies here may be required. Furthermore, the downstream ramps could potentially be actuated to provide direct control of the plume vorticity. More research is required in this area to fully assess the possibilities.

Reaction control rockets and scramjet fuel injectors entail dissimilar injection and combustion. Hence, it is recommended that the single-port studies be expanded to include both dissimilar gaseous injection and reacting flow gaseous injection to provide for more realistic simulations. The rugged stainless steel construction of the Mach 5.0 wind tunnel makes this facility uniquely appropriate for this effort.

Bibliography

Aerosoft, Inc., *GASP Version 3 Users' Manual,* Blacksburg, VA, 1999.

Abromovich, G., *The Theory of Turbulent Jets*, MIT Press, Cambridge, MA, 1960.

Andreopoulos, J. and Rodi, W., "Experimental Investigation of Jets in a Cross-flow," *J. Fluid Mech.*, Vol. 138, 1984, pp. 93-127.

Anderson, J., *Modern Compressible Flow with Historical Perspective, 2nd Ed.*, McGraw Hill, New York, 1990.

Alverez, J., Jones, W., and Seoud, R., "Predictions of Momentum and Scalar Fields in a Jet in a Cross-flow using First and Second Order Turbulence Closure," AGARD-CP-534, 1993, pp. 24.1-24.10.

Bowersox, R., Tucker, K., and Whitcomb, C., "Two-Dimensional Nonadiabatic Injection into a Supersonic Freestream," *Journal of Propulsion and Power,* March-April, 2000, pp. 234-242.

Bowersox, R., "Thermal Anemometry," *Handbook of Fluid Dynamics and Fluids Machinery,* ed. J. Schetz and W. Fuhs, John-Wiley, New York, 1996a, pp. 965-983.

Bowersox, R., "Combined Laser Doppler Velocimetry and Cross-Wire Anemometry Analysis for Supersonic Turbulent Flow," *AIAA J.,* Vol. 34, No. 11, 1996b, pp. 2269-2275.

Bowersox, R., "Turbulent Flow Structure Characterization of Angled Injection into a Supersonic Cross-flow," *J. of Spacecraft and Rockets*, Vol. 34, No. 2, 1996c, pp. 205-213.

Chenault, L., Beran, P., and Bowersox, R. "Numerical Investigation of Supersonic Injection Using a Reynolds-Stress Transport Model," *AIAA Journal*, Vol. 37, No. 10, 1999, pp. 1257-1269.

Chui, S., Karling, R., Margason, R., Tso, J., "A Numerical Investigation of a Subsonic Jet into a Cross-flow," AGARD-CP-534, 1993, pp. 22.1-22.14.

Drummond, P., "Suppression and Enhancement of Mixing in High-Speed Reacting Flow fields," *Combustion in High-Speed Flows*, Kluwer Acad. Press., 1994, pp. 191-229.

Fric, T. F. and Roshko, A., "Structure in the Near Field of the Transverse Jet," Proceedings of the Seventh Symposium on Turbulent Shear Flows, Vol. 1 (A90-35176), Aug. 1989, pp. 6.4.1-6.4.6.

Fric, T. and Roshko, A., "Vortical Structure in the Wake of a Transverse Jet,"*JFM*, Vol. 279, pp. 1-47. General Discussion, AGARD-CP-523, 1993, pp. GD.1-GD.13.

Fuller, E., Mays, R., Thomas, R., Schetz, J., "Mixing Studies of Helium in Air at High Supersonic Speeds," *AIAA Journal*, Vol. 30, No. 9., 1992, pp. 2234-2243.

Gessner, F., "The Origin of Secondary Flow in Turbulent Flow Along a Corner," *J. of Fluid Mechanics*, Vol. 58, Part 1., 1973, pp. 1-25.

Grasso, F., and V. Magi, "Simulation of Transverse Gas Injection in Turbulent Supersonic Air Flows", *AIAA Journal*, Vol. 33, No. 1, 1995, pp. 56-62.

Hinze, O., *Turbulence*, McGraw-Hill, 1975.

Holeman, J., *Heat Transfer 6th Ed.*, McGraw-Hill, New York, 1986.

Hollo, S. D., J. C. McDaniel and R. J. Harfield, "Quantitative Investigation of Compressible Mixing: Staged Transverse Injection into Mach 2 Flow", *AIAA Journal*,

Vol. 32, No. 3, 1994, pp. 528-534.

Kamotani, Y. and Greber, I., "Experiments on a Turbulent Jet in a Cross-flow," *AIAA J.*, Vol. 10, No. 11, 1972, pp. 1425-1429.

Kelso, R., Delo, C, and Smits, A., "Unsteady Wake Structures in Transverse Jets," AGARD-CP-534, 1993, pp. 4.1-8.

Keuthe, A. M., "Investigation of the Turbulent Mixing Regions Formed by Jets," *J. of Appl. Mech.,* Sept. 1935, pp. A-87-A-95.

Kovasznay, L., "Hot-Wire Anemometry in Supersonic Flow," *J. of Aeron. Sci.,* Vol. 17, 1950, pp. 565-584.

Lozano, A., Smith, S., Mungal, M., Hanson, R., "Concentration Measurements in a Transverse Jet by Planar Laser Induced Fluorescence of Acetone," *AIAA J.,* Vol. 32, 1994, pp. 218-221.

Margason, R. J., "Fifty Years of Jets in Cross-flow Research," AGARD-CP-534, Nov. 1993, pp. 1.1 - 1.41.

McCann, G. and Bowersox, R., "Experimental Investigation of Supersonic Gaseous Injection into a Supersonic Free stream," *AIAA J.,* Vol. 34, 1996, pp. 317-323.

Morrison, J., "A Compressible Navier-Stokes Solver with Two-Equation and Reynolds Stress Turbulence Closure," NASA CR-4440, May 1992.

Schetz J. A. and F. S. Billig, "Penetration of Gaseous Jets Injected into a Supersonic Stream", *Journal of Spacecraft and Rockets*, Vol. 3, No. 11, 1966, pp. 1658-1665.

Spangenberg, W., "Heat Loss Characteristics of Hot-Wire Anemometers at Various Densities in transonic and Supersonic Flow," NACA TN 3381, 1955.

United States Air Force, *New World Vistas, Air and Space Power for the 21ˢᵗ Century, Aircraft and Propulsion Volume,* 1995.

Wilcox, D. C., *Turbulence Modeling for CFD*, DCW Inc., La Canada, CA, 1993.

Wilson, M., Bowersox, R., and Glawe, D., "An Experimental Investigation of the Role of Downstream Ramps on a Supersonic Injection Plume," *Journal of Propulsion and Power,* Vol. 15, No. 3, 1998, pp. 432-439.

Table 1.1 Flow Conditions for the New Wind Tunnels

Mach No.	T_t (K)	T (K)	u (m/s)	p_t (MPa)	p (kPa)	Re /m	h_t (MJ/kg)	Run Time
4.9[1]	350-530	60-91	770-940	2.3-4.0	4.9-8.5	27-91	0.36-0.53	6.0 s
4.9[2]	355	61	770	2.4	5.1	55	0.36	6.0 s
7.0[3]	650-3300	100-300	1500-2400	5.9-20	1.4-4.8	2.2-29	1.2-3.2	2.0-5.0 ms

[1]Blow-Down Wind Tunnel Available Conditions, [2]Blow-Down Wind Tunnel Conditions for the Present Jet Interaction Research, [3]Computed Shock Tunnel Performance [Helium Gas Driver p = atm (2200 psia), T = 300 K)]

Table 1.2 Jet Interaction Test Matrix

Injector Geometry	M_j	α	p_{tj} (atm)	T_{tj} (K)	Re/m ($\times 10^6$)	u_j/u_∞	$\rho_j u_j^2/\rho_\infty u_\infty^2$ (J)	T_j/T_∞	Tt_j/Tt_∞	$\dot{m}_j/\dot{m}_\infty$
SP-D-NR[1]	1.0	10.0	1.0	295	15	0.41	0.43	4.0	0.83	0.0035
SP-D-NR	1.0	27.5	1.0	295	15	0.41	0.43	4.0	0.83	0.0035
SP-D-NR	1.0	45.0	1.0	295	15	0.41	0.43	4.0	0.83	0.0035
SP-D-NR	1.0	45.0	4.4	295	67	0.41	1.91	4.0	0.83	0.0122
SP-D-NR	1.0	45.0	5.8	295	90	0.41	2.59	4.0	0.83	0.0212
SP-D-NR	1.0	90.0	1.0	295	15	0.41	0.43	4.0	0.83	0.0035
SP-D-NR	1.0	90.0	4.4	295	67	0.41	1.91	4.0	0.83	0.0122
SP-D-NR	1.0	135.0	1.0	295	15	0.41	0.43	4.0	0.83	0.0035
SP-C-NR[2]	1.0	90.0	1.0	295	15	0.41	0.43	4.0	0.83	0.0035
SP-C-NR	1.0	90.0	4.4	295	67	0.41	1.91	4.0	0.83	0.0122
SP-D-TR[3]	1.0	45.0	1.0	295	15	0.41	0.43	4.0	0.83	0.0035
DA-D-NR[4]	1.0	45.0	1.0	295	15	0.41	0.43	4.0	0.83	0.0862

[1]SP-D-NR => Single-Port Diamond Injector with No Ramp present, [2]SP-C-NR => Single-Port Circular Injector with No Ramp present, [3]SP-D-DR/TR => Single-Port Diamond Injector with the Tapered Ramp present, and [4]DA-D-NR => Distributed Array Diamond Injector with No Ramps present and the mass flow rate was for all 64 injectors.

Table 1.3 Project Timeline

Task ↓ / Month →	2 98	5 98	8 98	11 98	2 99	5 99	8 99	11 99	2 00	5 00	8 00	11 00
Thrust 1 – Laboratory Development												
Mach 5 Tunnel	●——		●		●—●							
Shock Tunnel	●———————————————————————————————→											
New Flow Straightner											●●	
New Low-Re Calibration Facility										●—●	●	
Thrust 2 – Jet Interaction Studies												
Single-Port Injection												
Model Fabrication						●—●						
PIV/Flow Visualization							●—●					
PSP								●———————————————————————●				
Five-Hole Probe												→
Cross-Wire Anemometry												
Distributed Array Injection												
Model Fabrication										●—●		
Surface Oil Flow / Schlieren											●	
Five-Hole Probe											●	
Numerical Simulations												
Current Modeling Assessment										●———→		
New Model Development												→
Write Final Report Due												●

●— Start, —●End, —→ Continuing

Table 3.1 Measurement Uncertainties[1]

Measurement	Unc.
$P_{t\infty}$ (kPa)	20.
$T_{t\infty}$ (K)	3.0
x/d	0.3
y/d	0.1
$\overline{\rho u} / \rho_e u_e$	0.04
$\sqrt{\overline{(\rho u)'^2}} / \overline{\rho u}$	0.006
$\sqrt{\overline{(\rho v)'^2}} / \overline{\rho u}$	0.005
$\sqrt{\overline{(\rho w)'^2}} / \overline{\rho u}$	0.005
$\overline{(\rho u)'(\rho v)'} / \overline{\rho u}^2$	0.0005
$\overline{(\rho u)'(\rho w)'} / \overline{\rho u}^2$	0.0005
$\overline{(\rho u)'(T_t)'} / \overline{\rho u}^2$	0.0005
$\overline{(\rho v)'(T_t)'} / \overline{\rho u}^2$	0.0005
$\overline{(\rho w)'(T_t)'} / \overline{\rho u}^2$	0.0005
Pressure Sensitive Paint (psi)	0.15
Pitot Pressure (kPa)	500
Cone-Static Pressure (kPa)	300
Mach Number (Pitot Pressure, $M = 5.0$)	0.01
Mach Number (Five-Hole Probe, $M = 2$)	0.02
Mach Number (Five-Hole Probe, $M = 3$)	0.05
Mach Number (Five-Hole Probe, $M = 4$)	0.10
Mach Number (Five-Hole Probe, $M = 5$)	0.20
Mach Number (Five-Hole Probe, $M = 6$)	0.30
Mach Number (Five-Hole Probe, $M = 7$)	0.45
Mach Number (Five-Hole Probe, $M = 8$)	0.65

[1]Standard Euclidean norm based analysis accounting for instrument uncertainty (supplied by manufacturer), calibration errors, position uncertainty and repeatability. Turbulence uncertainties were based on the analysis of Latin and Bowersox (2000).

Table 3.2 Five-Hole-Probe Calibration

Mach	P_c/P_{t2} [1]	%error [2]
1.20	0.6284	0.85
1.30	0.5491	0.73
1.40	0.4980	0.37
1.50	0.4568	0.47
1.75	0.3794	0.62
2.00	0.3256	0.20
2.25	0.2868	0.07
2.50	0.2580	0.02
2.75	0.2359	0.25
3.00	0.2187	0.50
3.25	0.2051	0.68
3.50	0.1941	0.71
4.00	0.1777	0.42
4.50	0.1661	0.36
5.00	0.1580	0.79
6.00	0.1470	1.13
7.00	0.1402	1.21
8.00	0.1357	0.60
9.00	0.1325	0.74
10.00	0.1300	0.91

[1]Theory: Exact for M≤5 and 10.0, Hypersonic Similarity for M = 6-9 (Difference between exact and Hypersonic Similarity < 0.5% at M = 5.0 and 10.0), [2]In Calibration Curve Fit.

Table 4.1 Single-Port-Injector Performance Estimates

α	M_1	p_{eff}/p_∞[2]	p_{eff}/p_∞[3]	p_{eff}/p_∞	$p_{t2}/p_{t\infty}$
10	2.6	1.4	1.1	**	0.9[6]
27.5	2.3	1.3	1.3	**	0.5[6]
45	1.8	1.2	1.3	**	0.2[6]
90	**	**	1.4	2.0[4], 1.6[5]	0.07[7]
135	**	**	**	2.0[4]	0.07[7]
90[1]	**	**	1.4	2.0[4]	0.07[7]

[1]Circular injector, [2]p_{eff} was calculated using shock-expansion theory, with the shock angles measured from the surface oil flow, as the average pressure around the circumference of the diamond orifice, [3]p_{eff} was computed, as the average pressure around the periphery of the exit port, from the pressure sensitive paint results, [4]Normal injection formula, $p_{eff} = 0.8p_2$, [5]Numerical simulation result. [6]Three-dimensional oblique shock theory, where the shock shape was measured and the free stream Mach number was assumed, [7]Normal shock result.

Table 4.2 Plume Penetration and Size

Injector Geometry	α	$\rho_j u_j^2 / \rho_\infty u_\infty^2$ (J)	y_{max}/d (x/d = 5.0)	y_{max}/d (x/d =21)	A_p/d^2 (x/d =21)
SP-D-NR[1]	10	0.43	1.9	2.8	6.2
SP-D-NR	27.5	0.43	2.4	3.0	7.1
SP-D-NR	45	0.43	2.6	3.0	7.1
SP-D-NR	45	1.91		4.0	13.
SP-D-NR	45	2.59		4.5	16.
SP-D-NR	90	0.43	3.2, 3.0[5]	3.5, 4.5[5]	9.6, 16
SP-D-NR	90	1.91		4.6	17.
SP-D-NR	135	0.43		3.8	11.
SP-C-NR[2]	90	0.43	3.0	3.2	8.0
SP-C-NR	90	1.91		5.0	20.
SP-D-TR[3]	45	0.43		3.4	9.1

[1]SP-D-NR => Single-Port Diamond Injector with No Ramp present, [2]SP-C-NR => Single-Port Circular Injector with No Ramp present, [3]SP-D-DR/TR => Single-Port Diamond Injector with the Double/Tapered Ramp present, and [4]DA-D-NR => Distributed Array Diamond Injector with No Ramps present and the mass flow rate was for all 64 injectors. [5]Numerical simulation results.

M = 5.0

(a)

M = 5.0

(b)
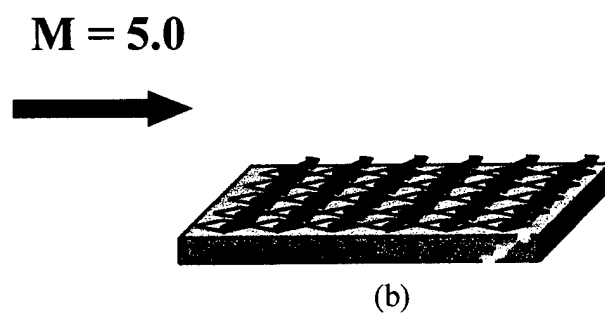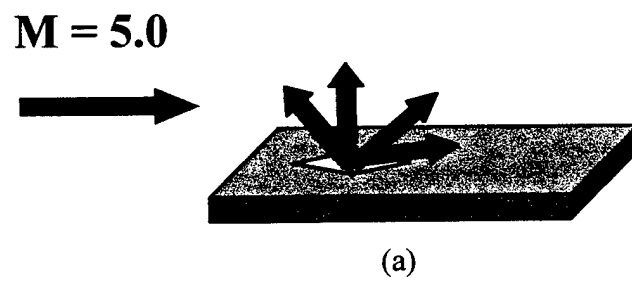
Fig. 1.1 Flow Field Schematics (a) Diamond Single-Port Injector, (b) Distributed Array Injector

⊕ M = 5.0 (Out of Page)

Boundary Layer Edge

Curved Isotach => Corner Flow Vorticity

Corner Flow Vorticity

Jet Plumes
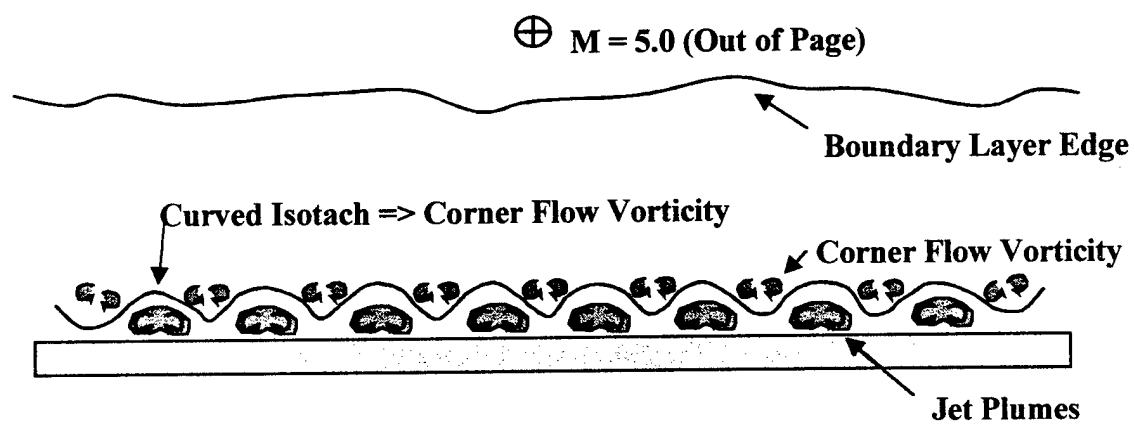
Fig. 1.2 Distributed-Array-Injector Concept
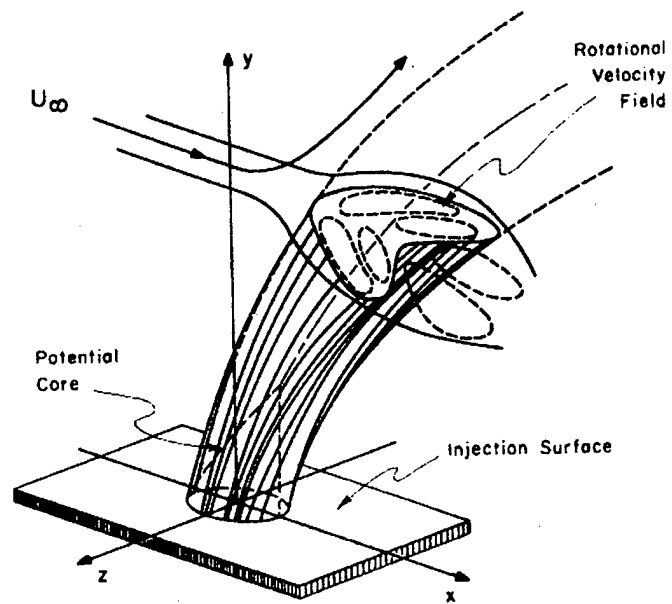
Fig. 2.1 Low-Speed Jet-Interaction Schematic [Abromovich (1960)]
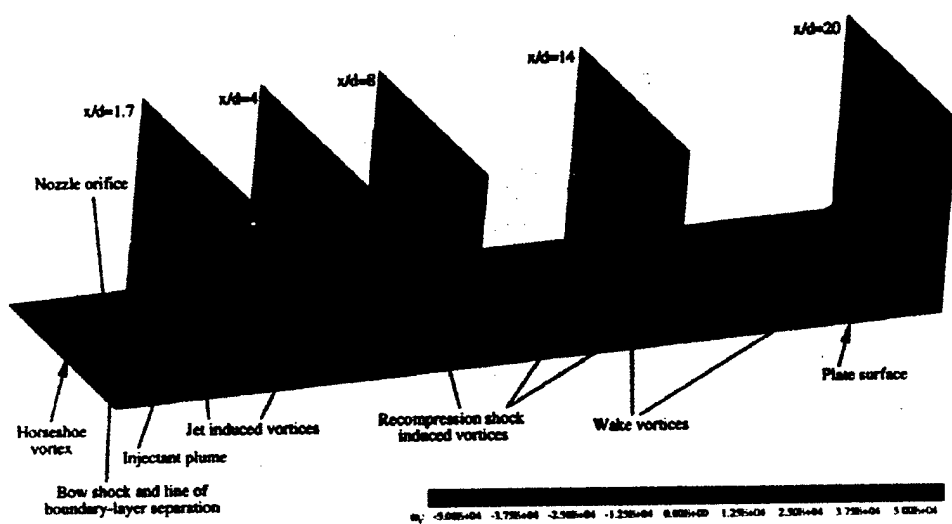
Figure 62. RSTM predictions of ω_x for McCann and Bowersox configuration

Fig. 2.2 High-Speed Jet-Interaction Vorticity Distribution [Chenault, Beran and Bowersox (1999)]
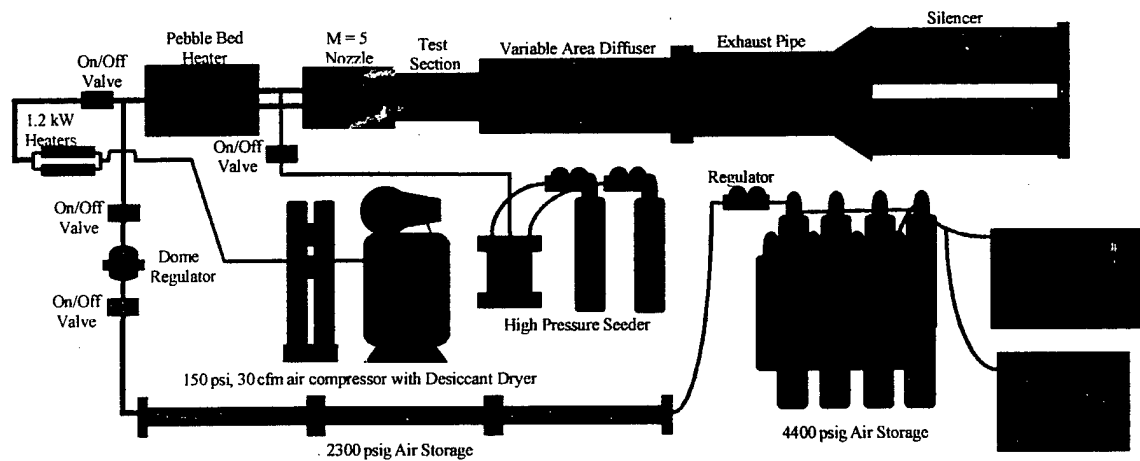
(a) Facility Schematic
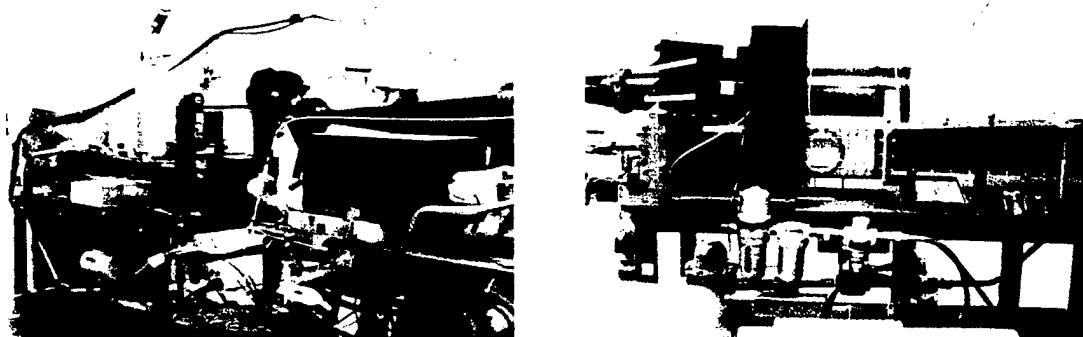
(b) Photographs

3.1 Mach 5.0 Wind Tunnel
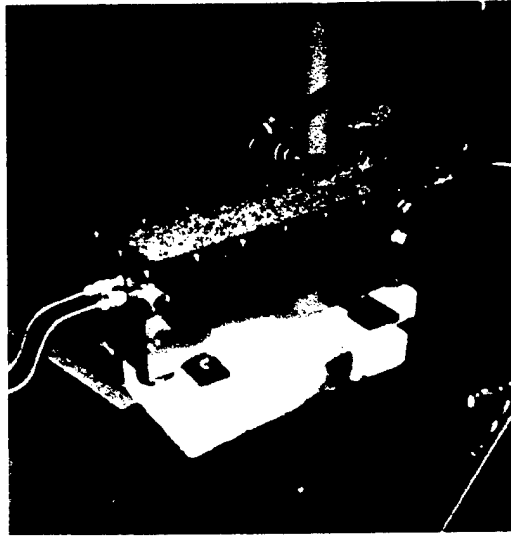
(a)
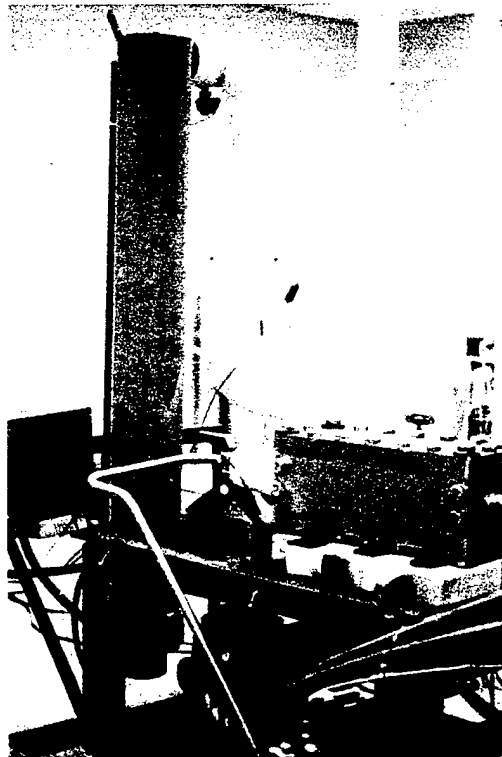
(b)

Fig. 3.2 Photographs of Pebble Bed Heater, (a) with the Top Removed, (b) Pebble Bed
with Electric Air Heater
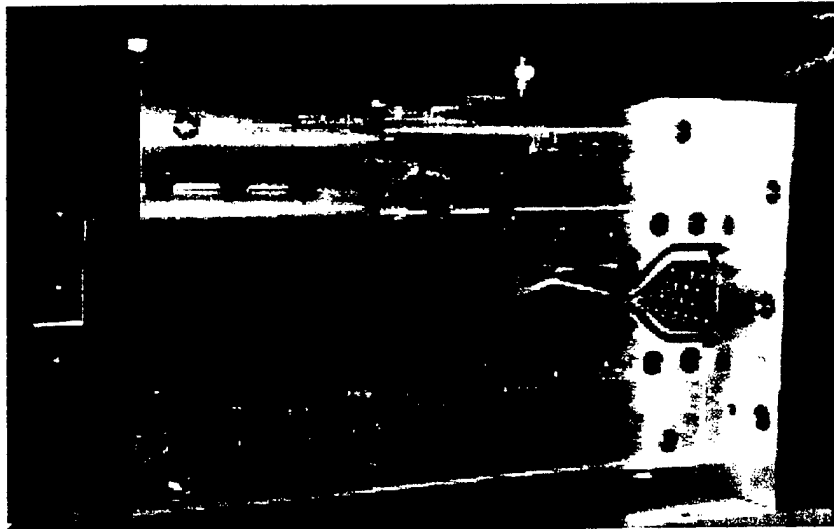
(a) Sidewall Removed with Old Aerogrid
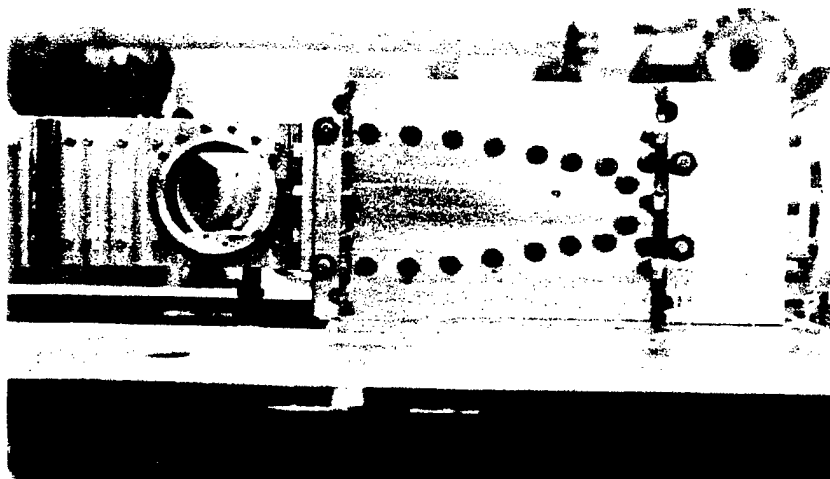
(b) Sidewall and New Flow Straightner In-Place

Fig 3.3 Photographs of the Mach 5.0 Contoured Nozzle

Flow Straightner Part #1:
8-Inch Thick Stainless Steel Insert
with New Aerogrids on Each Side

Flow Straightner Part 2
2-Inch Thick Stainless Steel Insert
with Turbulence Dampening Screen

New Aerogrids
on each side

Old Aerogrid

Turbulence
Dampening
Screen
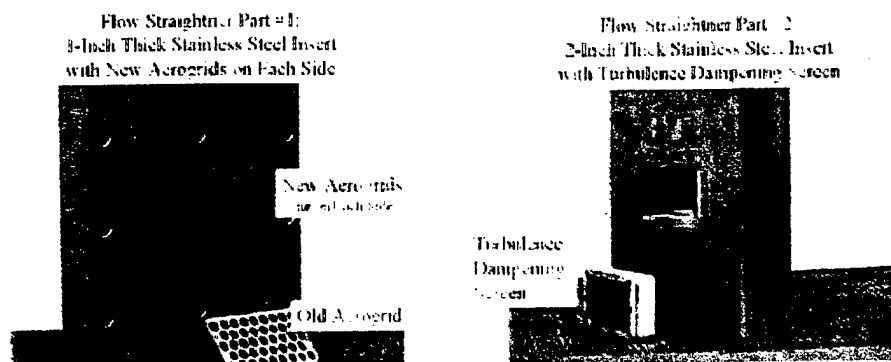
(a) Photographs
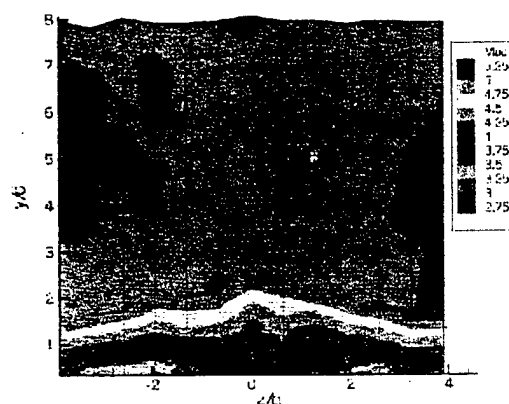
(b) Tunnel Calibration with Old Straightner
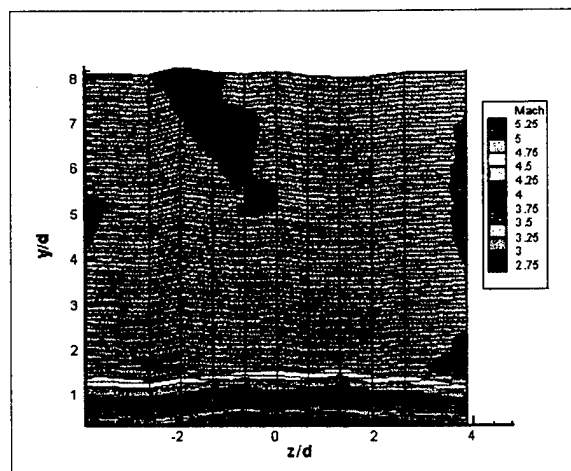
(c) Tunnel Calibration with New Straightner

Figure 3.4 New Flow Straightner

7.62 cm

7.62 cm

Test Section
Entrance

26.67 cm

Mach 5.0
Flow

7.13 cm

Injection Port
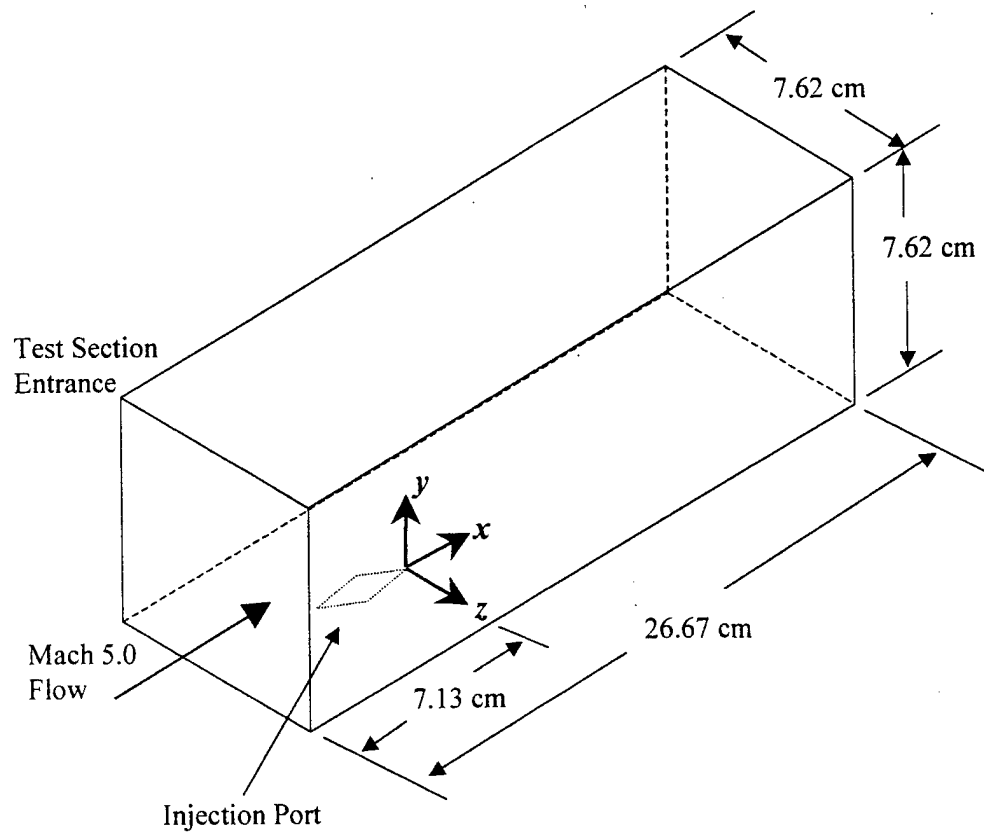
Fig. 3.5 Single-Port Test Section Geometry and Coordinate System
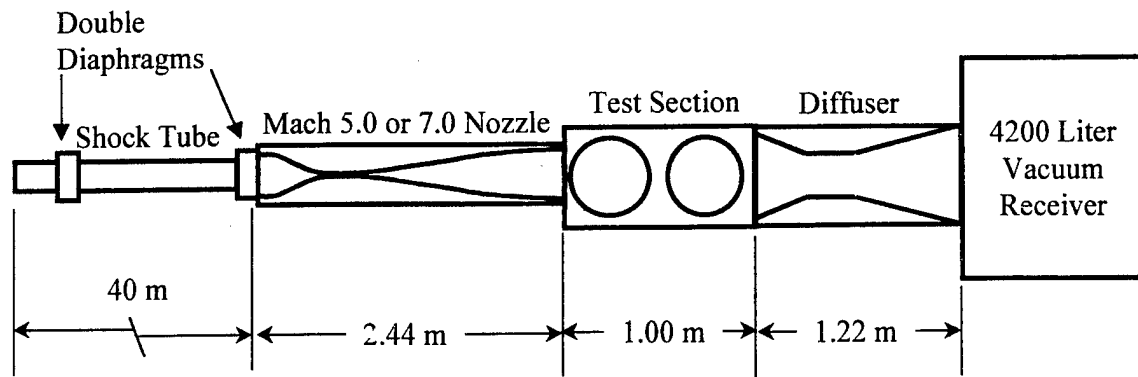
(a) Schematic
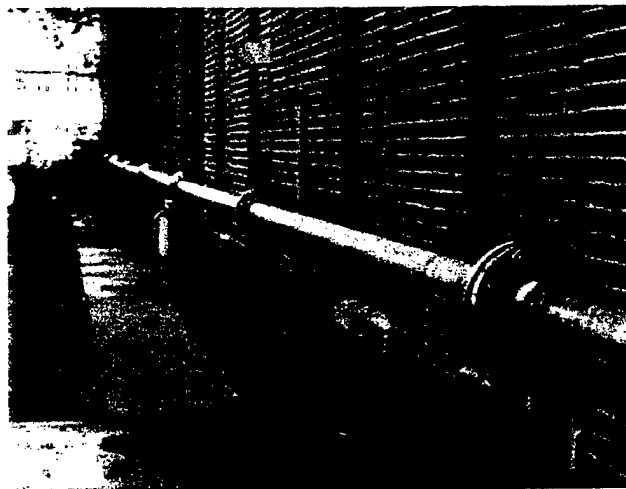
(b) Shock Tube
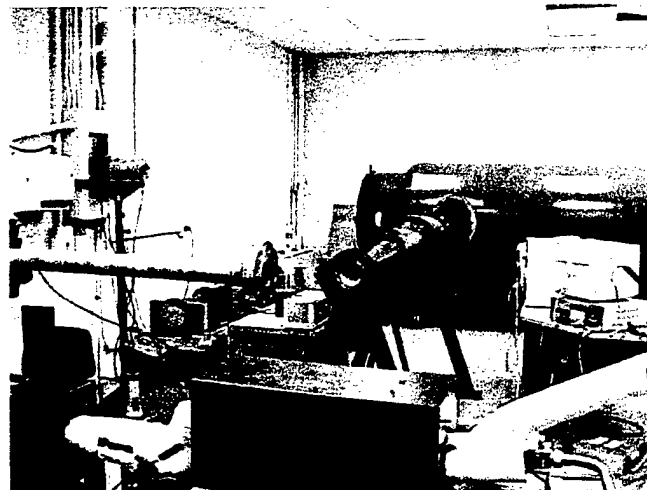
(c) Shock Tunnel Mach 7 Nozzle and Vacuum Receiver Tank
Fig. 3.6 Shock Tunnel Facility
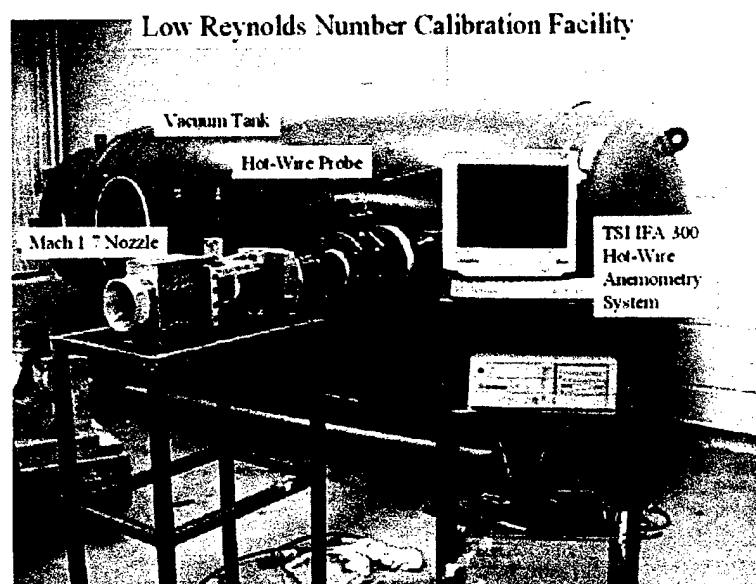
Fig. 3.7 Low Reynolds Number Calibration Facility

Top View

0.51 1.19 0.56

2.83

0.79
0.32
0.79

1.91

Side View

5.08

0.51

45 degrees

15 degrees

0.32

1.19

Enlarged View of the Diamond Hole
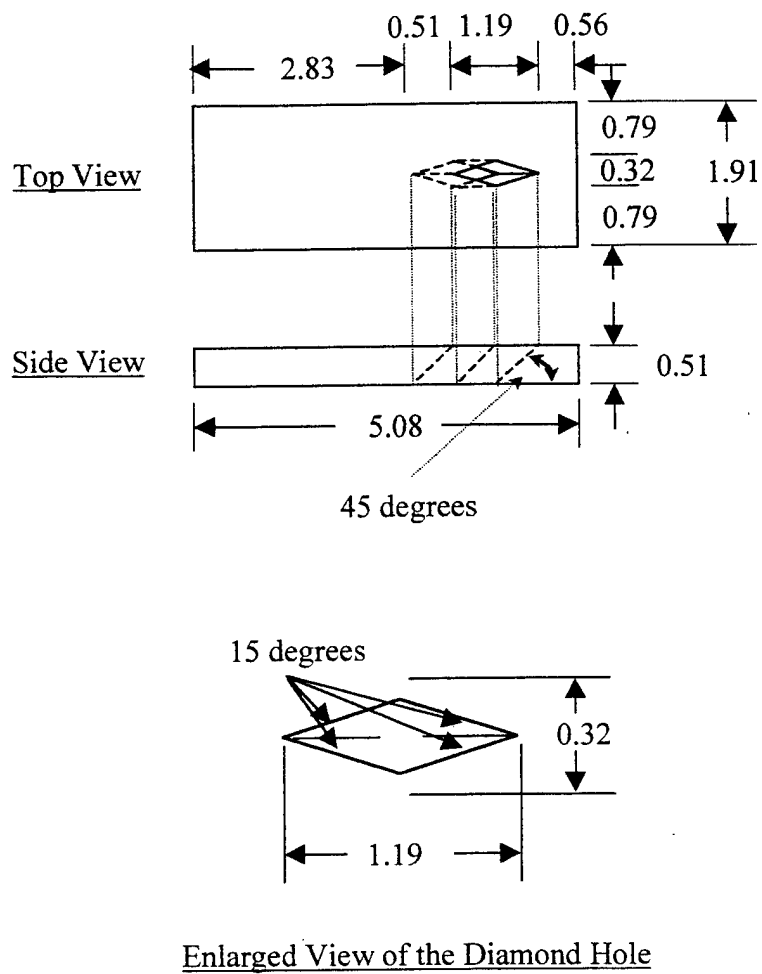
Fig. 3.8 Schematic of the Single Port Injector (45° Injector Shown)

Top view

0.83 cm

1.66 cm

1.45 cm

Front view

0.83 cm

1.45 cm

Side view

0.83 cm

45°

1.66 cm
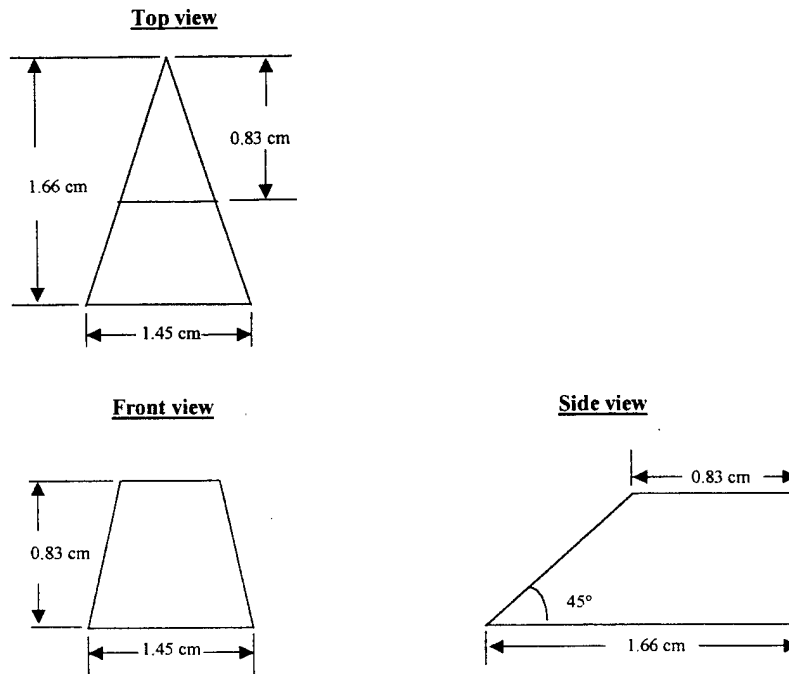
Fig. 3.9 Schematic of Variable Wall Tapered Ramp
[Design Based on Wilson, Bowersox and Glawe (1998)].
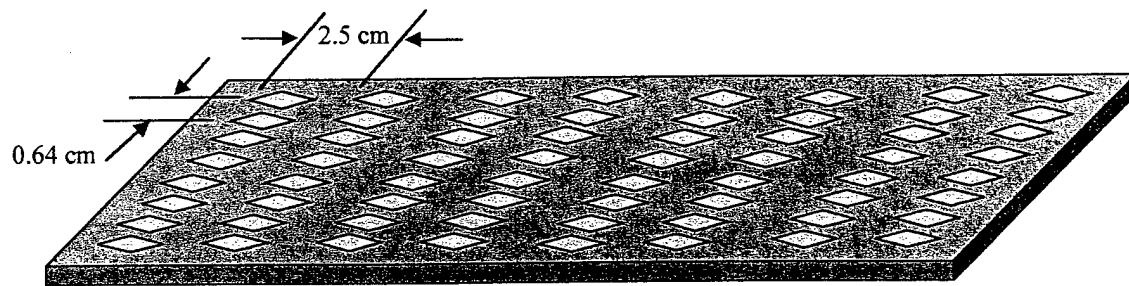
(a) Schematic of the Injector Layout
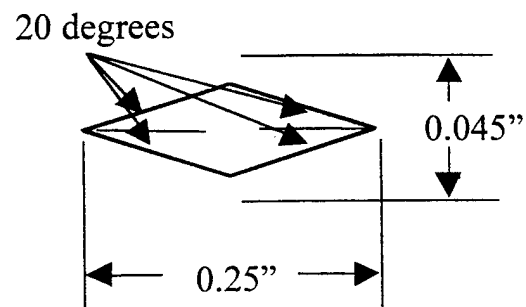
(b) Injector Geometry

Fig. 3.10 Distributed-Array-Injector
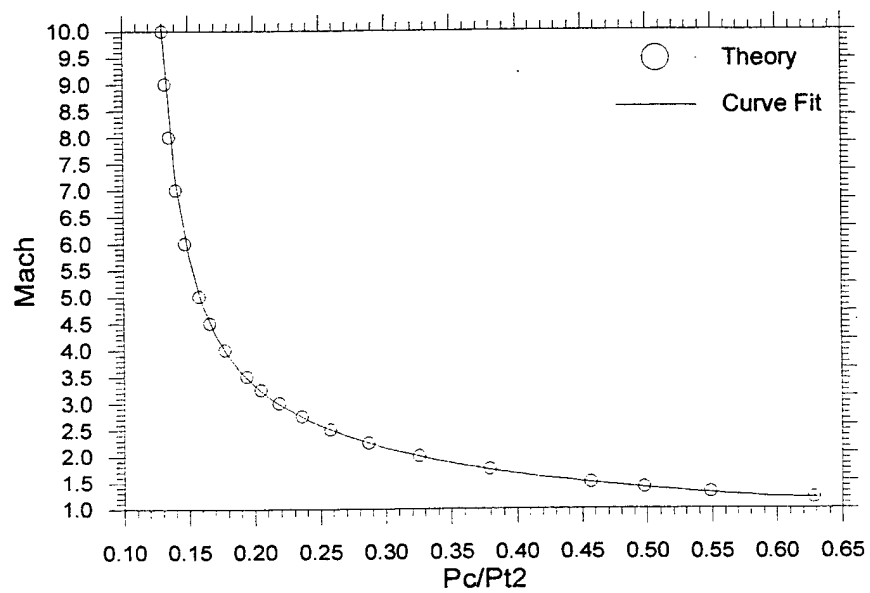
Fig. 3.11 Five-Hole-Probe Calibration
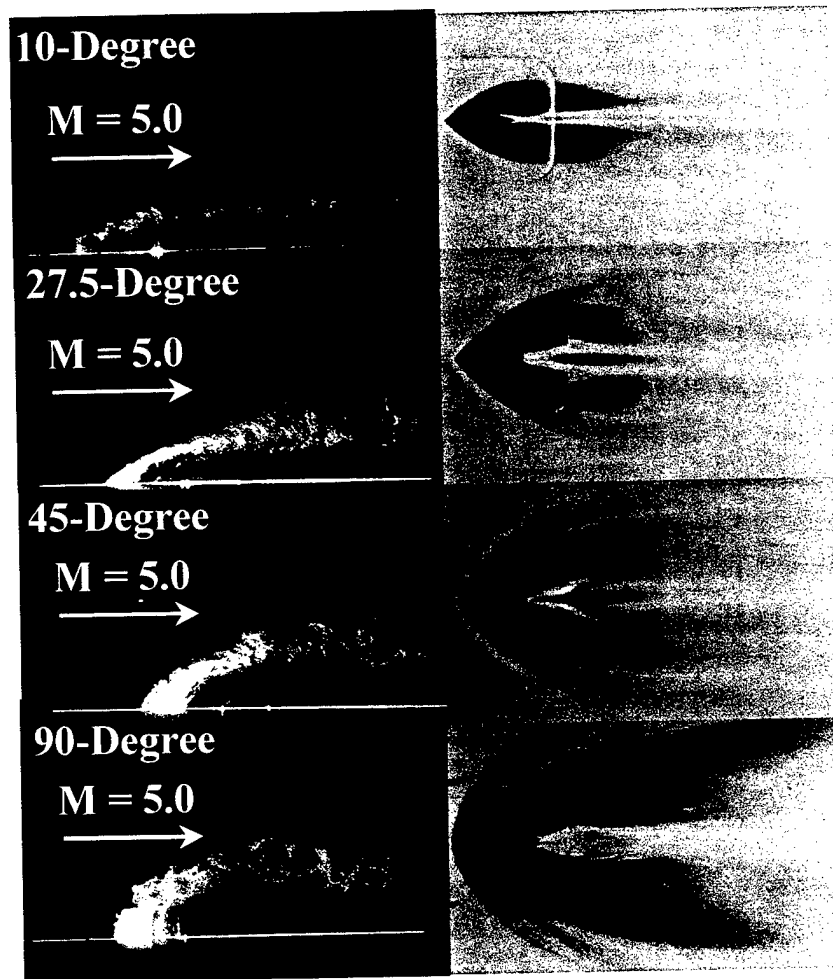
(a) Diamond 10-90° (*J* = 0.43)
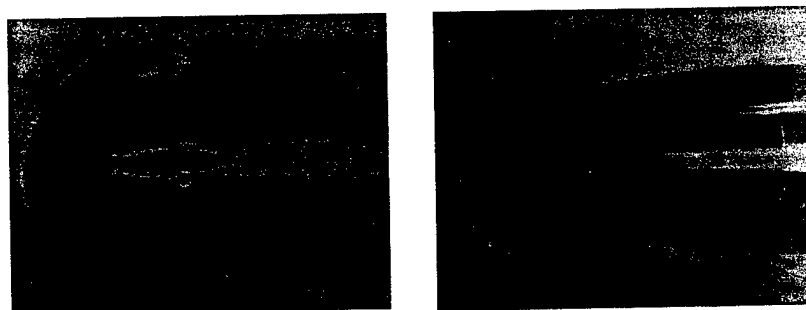
(b) Circular 90° and Diamond 135° (*J* = 0.43)

Fig. 4.1 Surface Oil and Mie Scattering Flow Visualizations
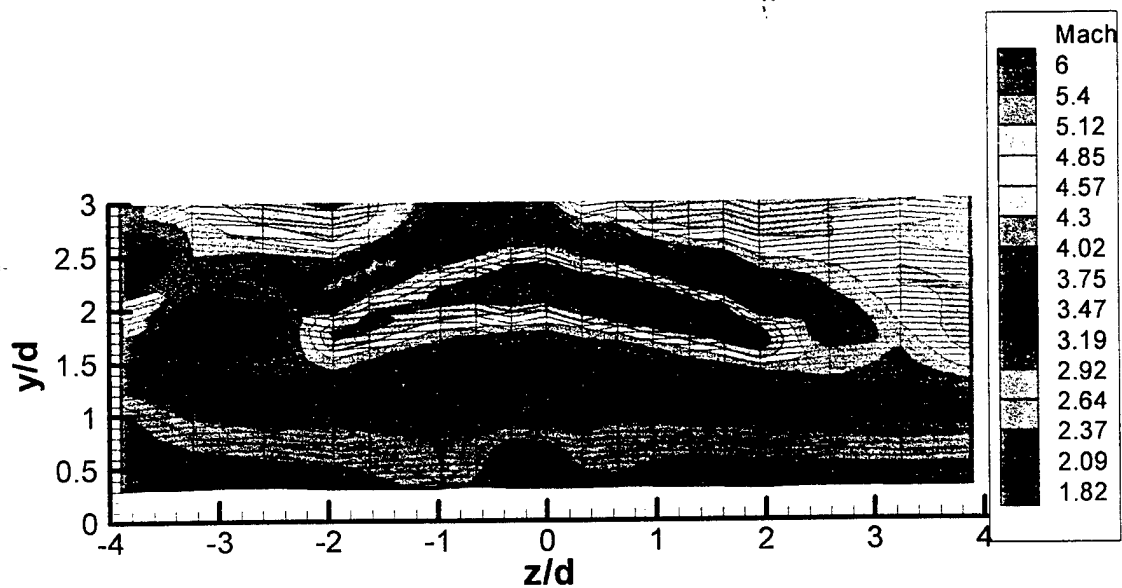
(a) 10° Diamond
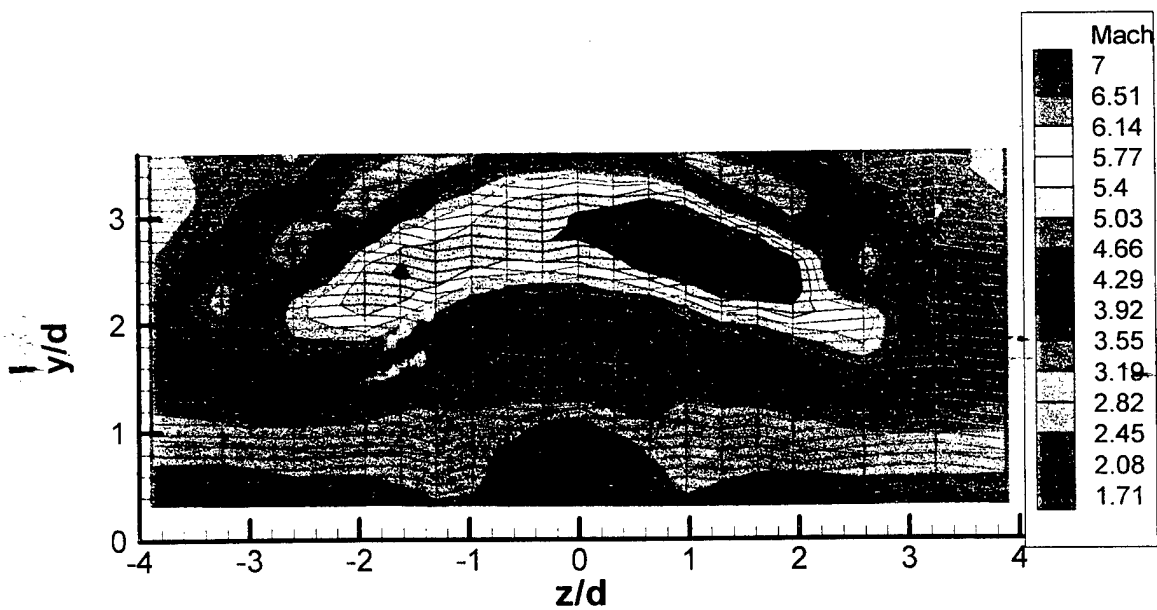
(b) 27.5° Diamond
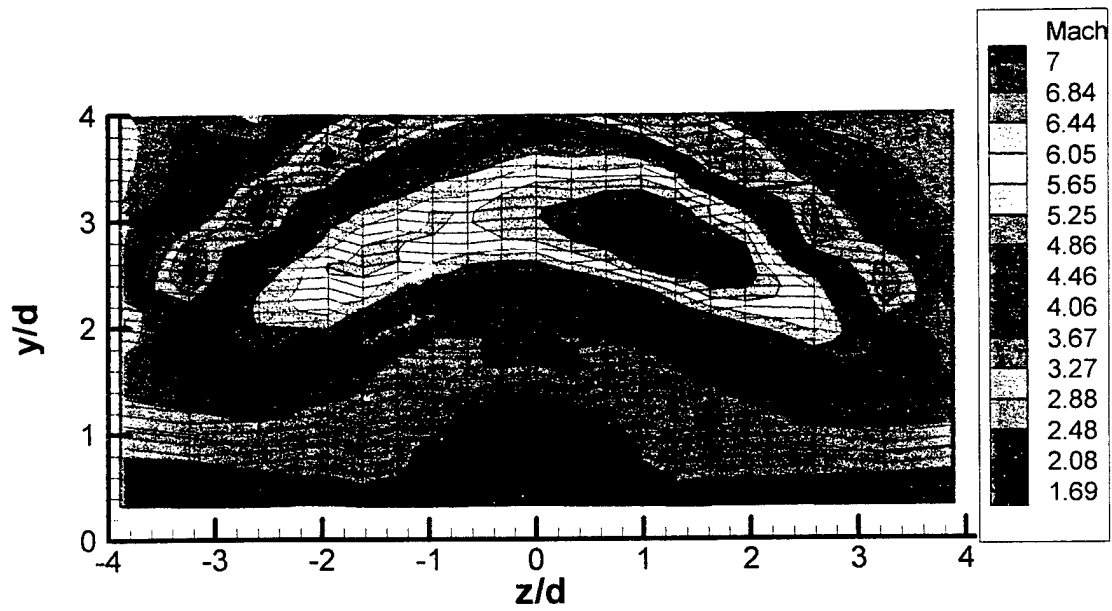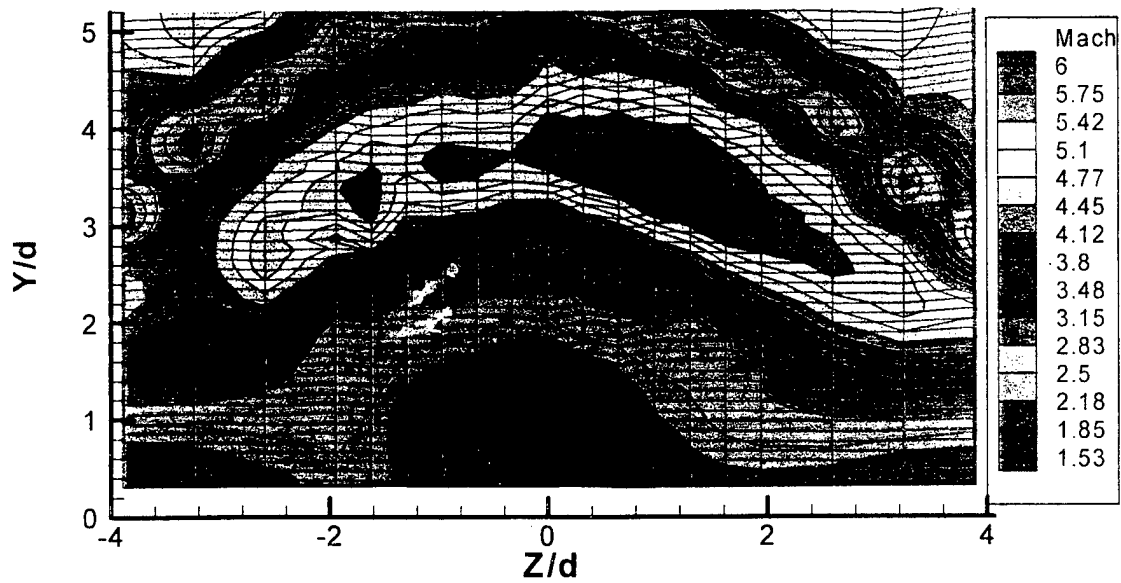
(c) 45° Diamond
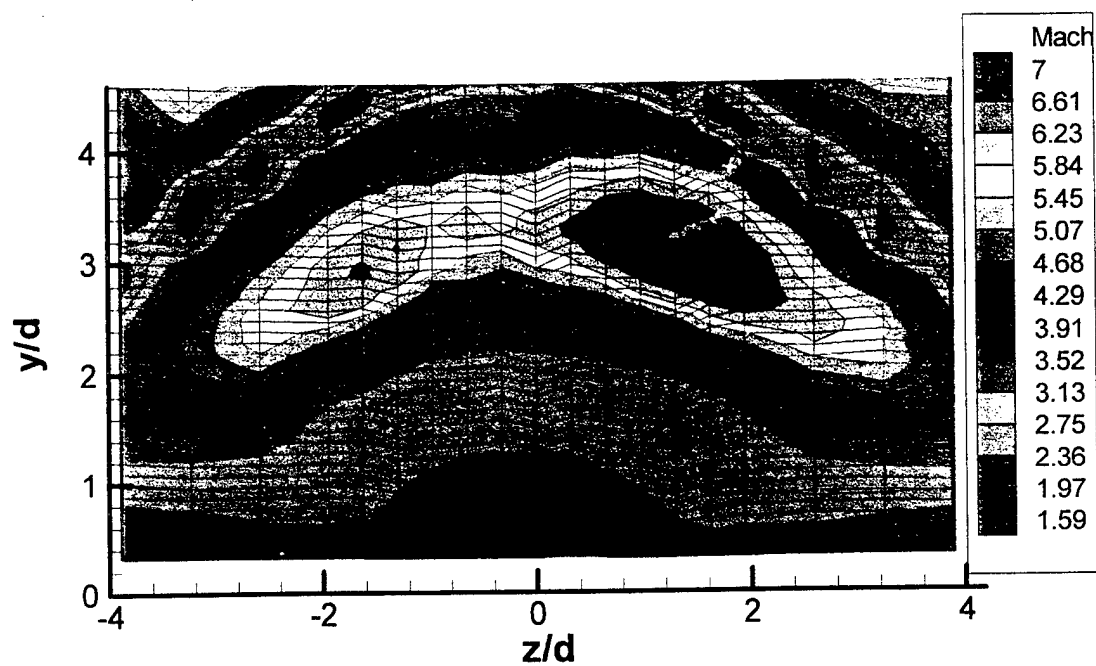
(d) 90° Diamond

(e) 90° Circular

Fig. 4.2 Mach Number Contours for the Single-Port Injectors (x/d = 5.0, J = 0.43)
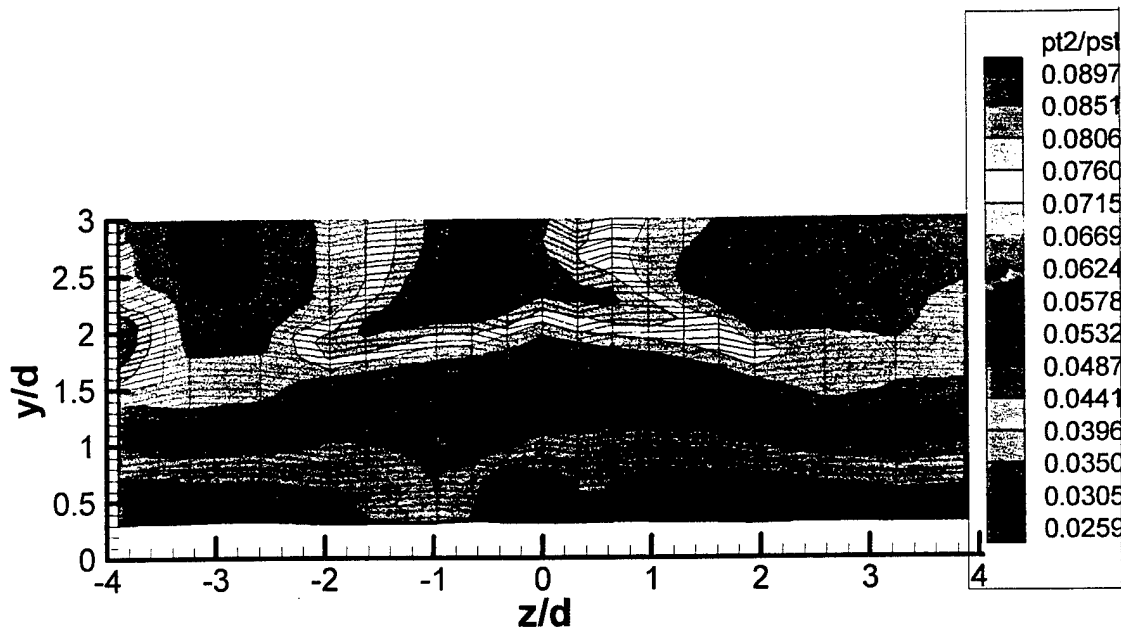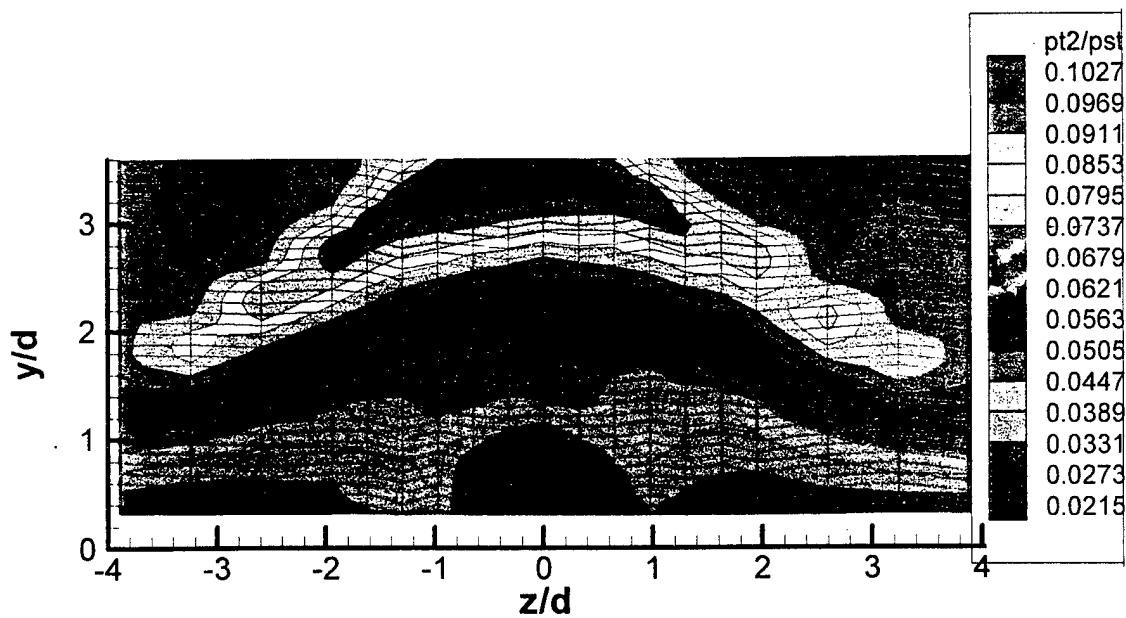
(a) 10° Diamond

(b) 27.5° Diamond
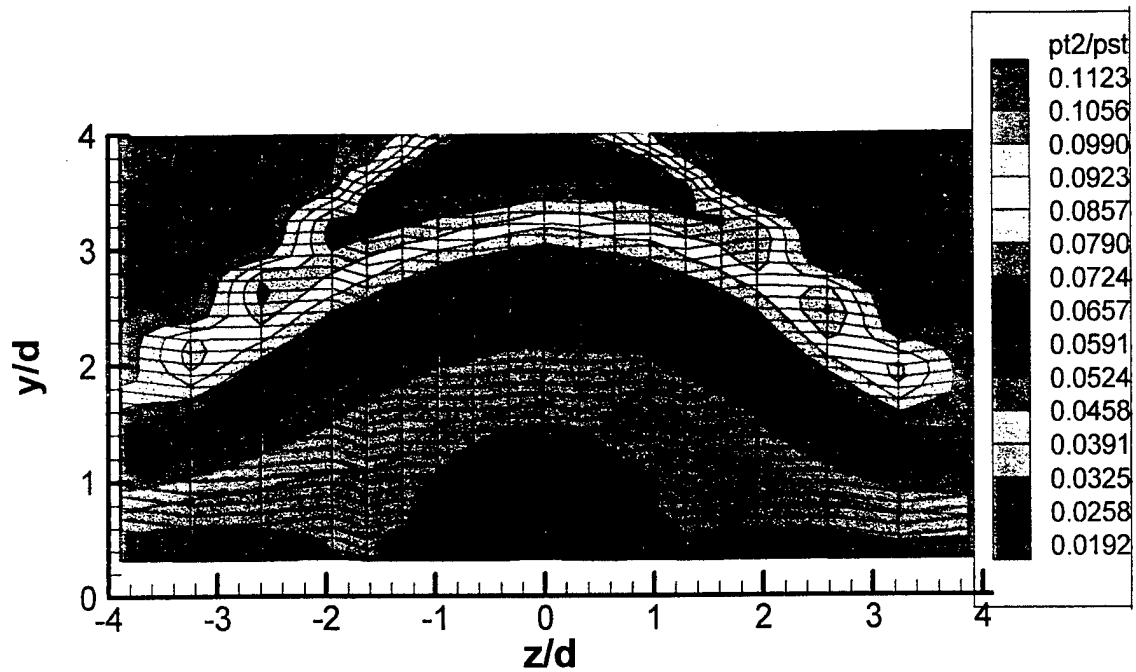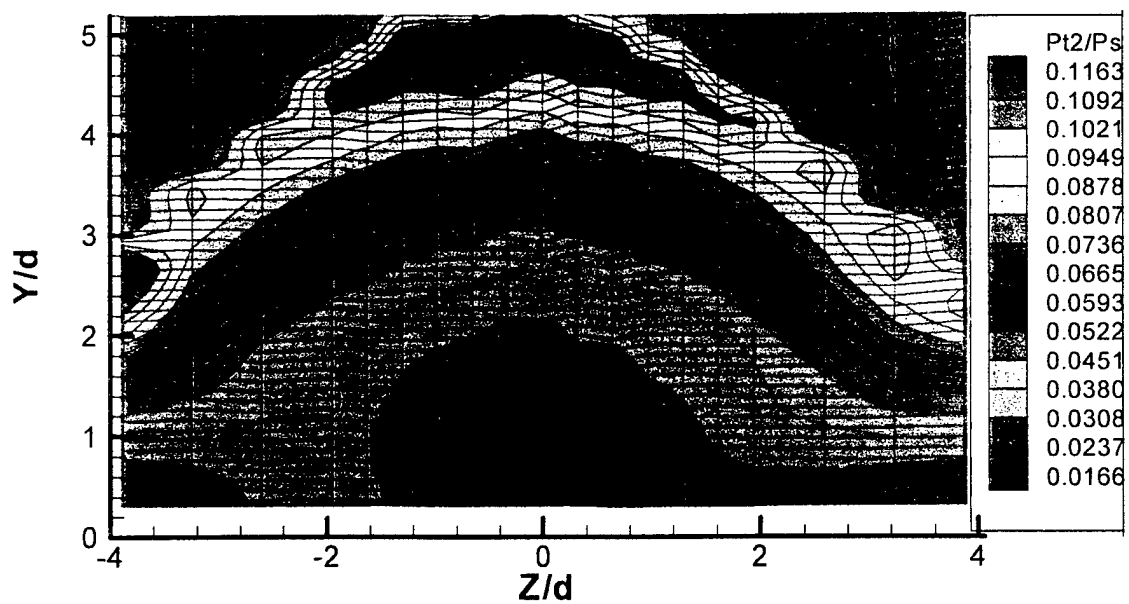
(c) 45° Diamond
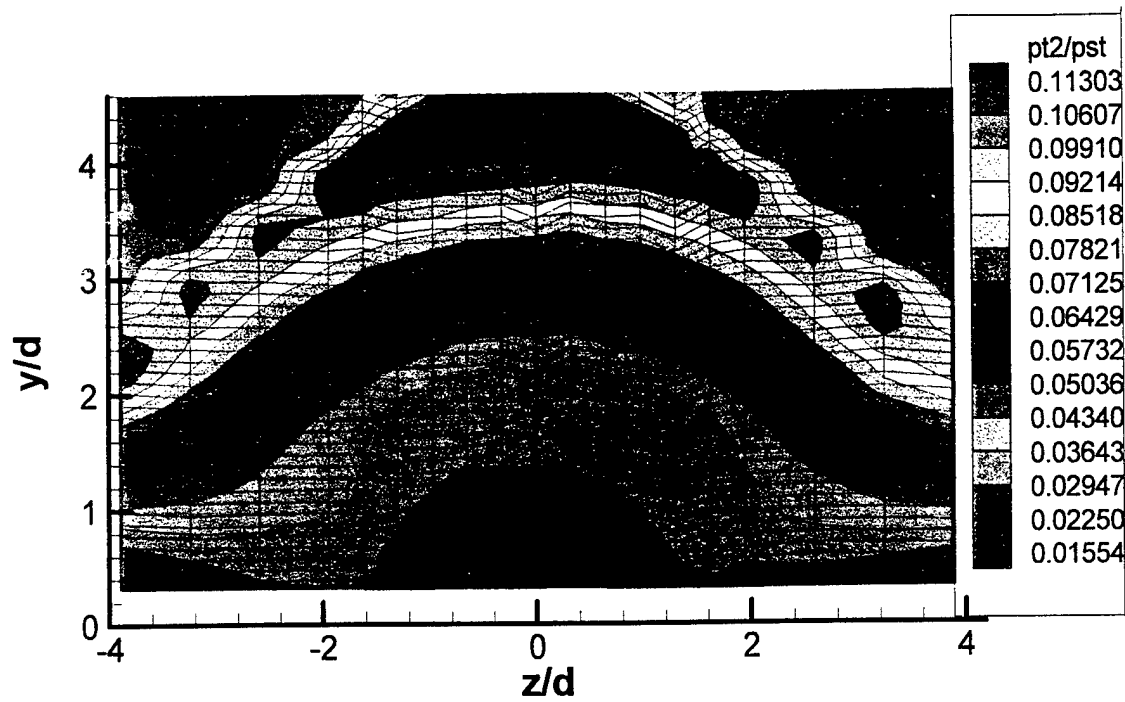
(d) 90° Diamond

(e) 90° Circular

Fig. 4.3 Pitot-Pressure Ratio ($P_{t2}/P_{t\infty}$) Contours for the Single-Port Injectors
($x/d = 5.0$, $J = 0.43$)
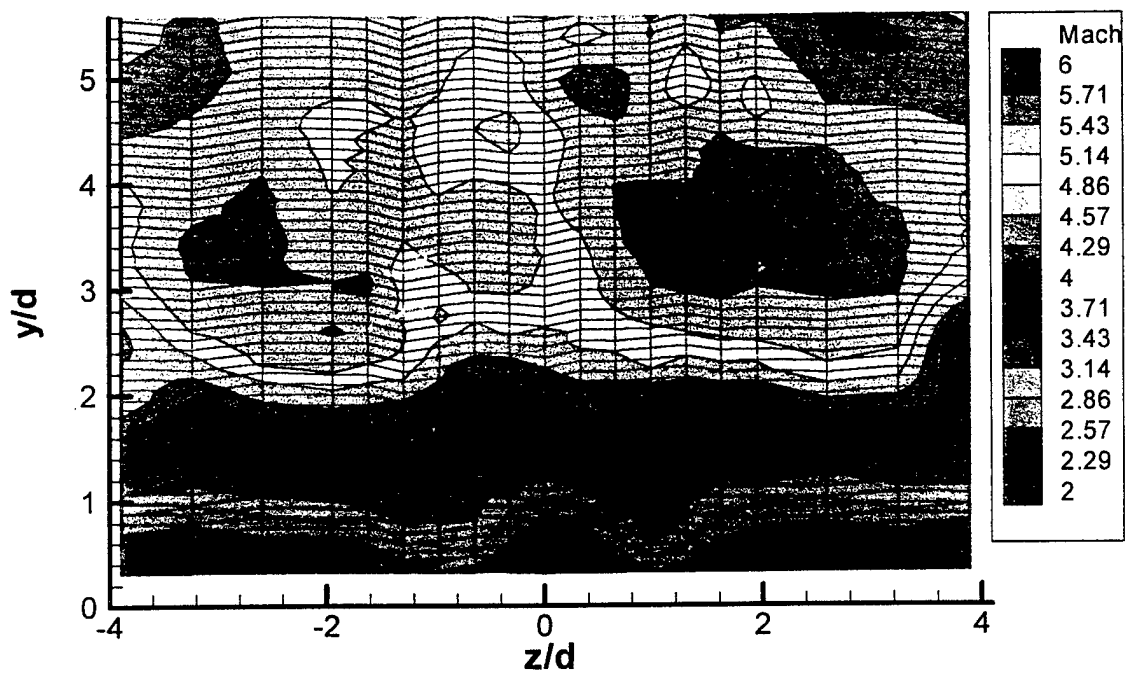
(a) 10° Diamond ($J = 0.43$)
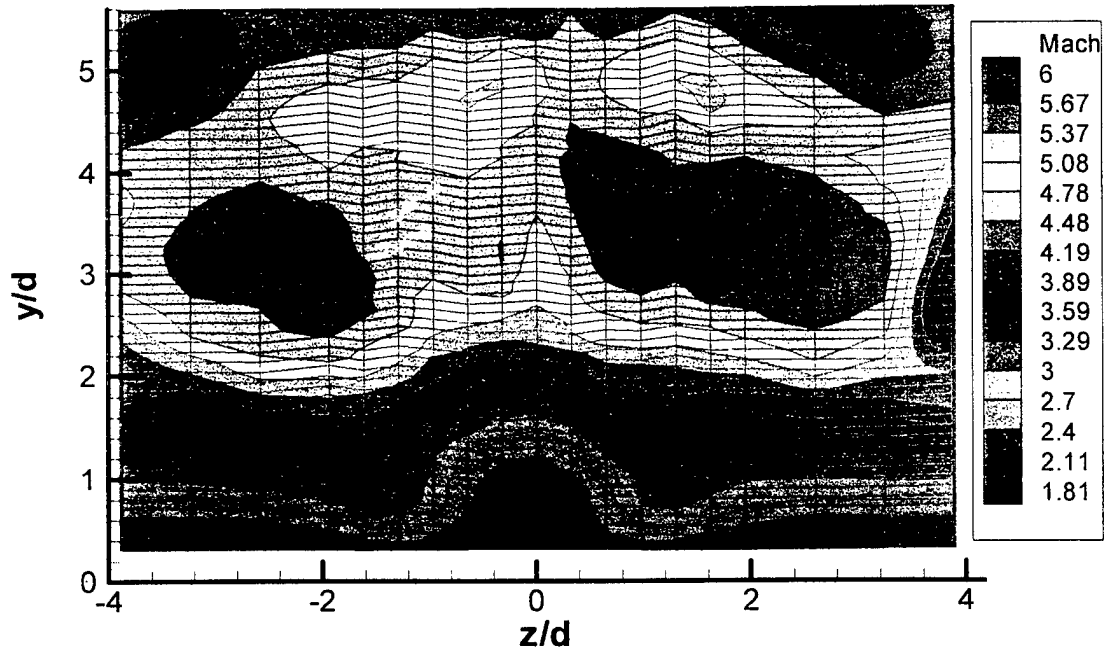
(b) 27.5° Diamond ($J = 0.43$)
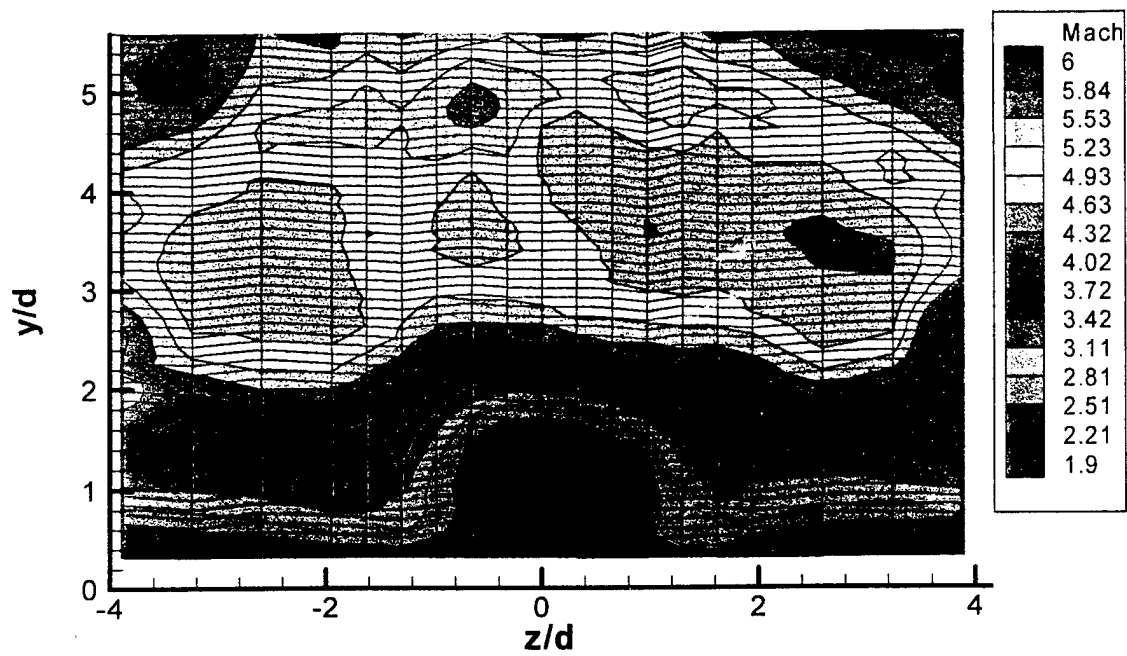
90

(c) 45° Diamond ($J = 0.43$)

(d) 90° Diamond ($J = 0.43$)

(e) 135°Diamond (*J* = 0.43)

(f) 90° Circular (*J* = 0.43)

92

(g) 45° Diamond ($J = 1.91$)

(h) 90° Diamond ($J = 1.91$)

93

(i) 90° Circular ($J = 1.91$)

(j) 45° Diamond ($J = 2.59$)

Fig. 4.4 Mach Number Contours for the Single-Port Injectors ($x/d = 21$)

(a) 10° Diamond ($J = 0.43$)

(b) 27.5° Diamond ($J = 0.43$)

95

(c) 45° Diamond ($J = 0.43$)

(d) 90° Diamond ($J = 0.43$)

(e) 135°Diamond ($J = 0.43$)

(f) 90° Circular ($J = 0.43$)

97
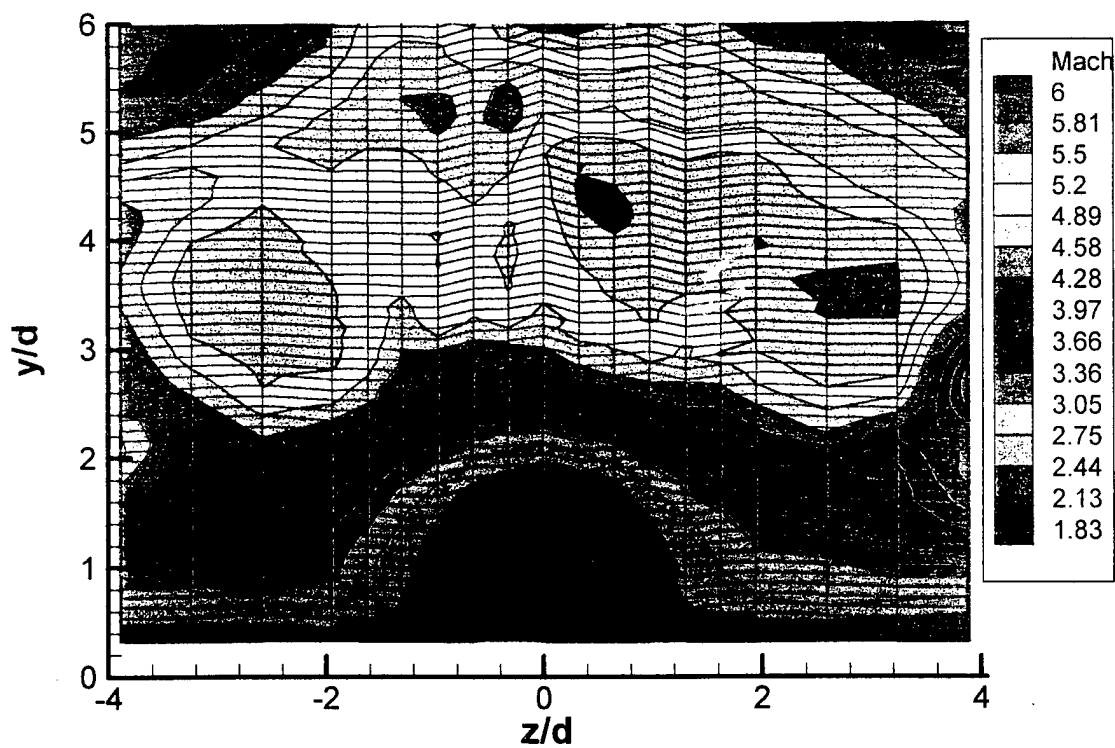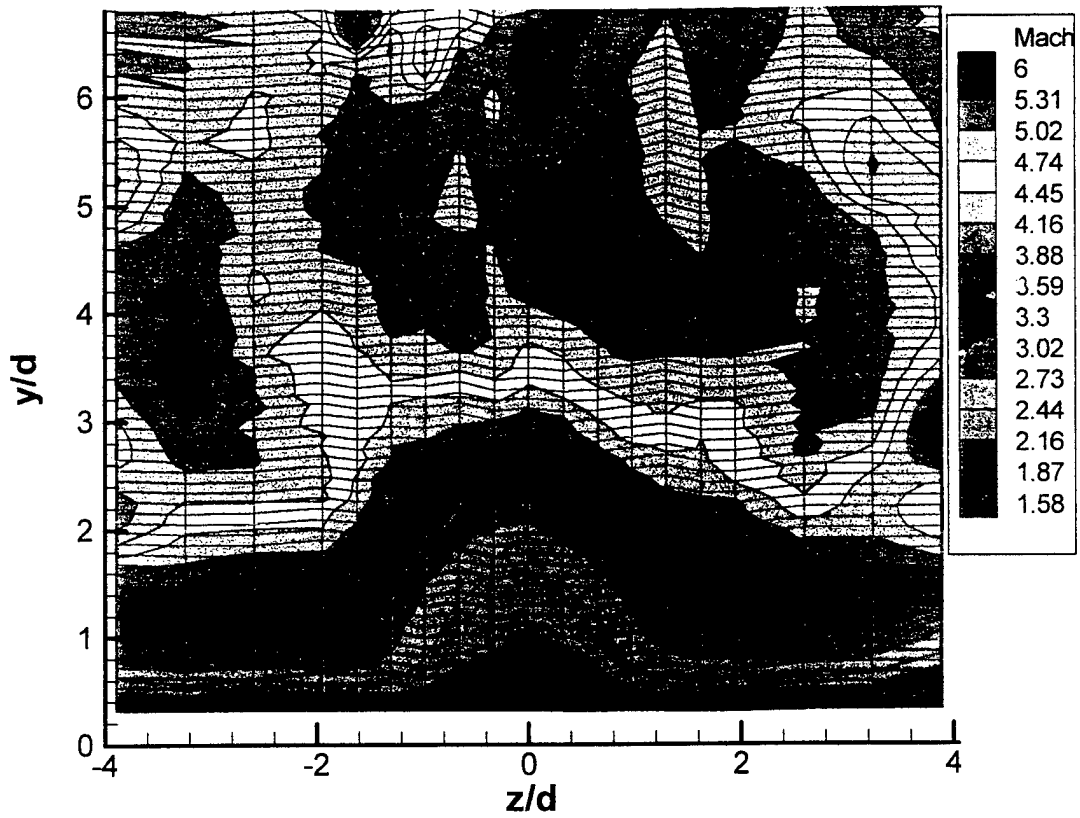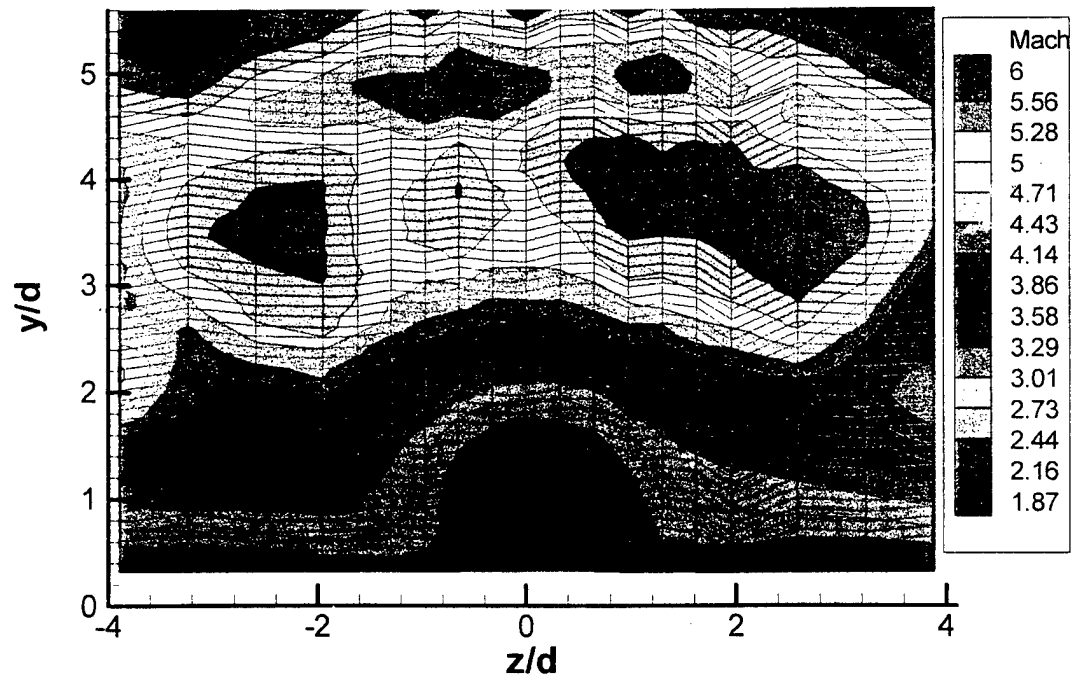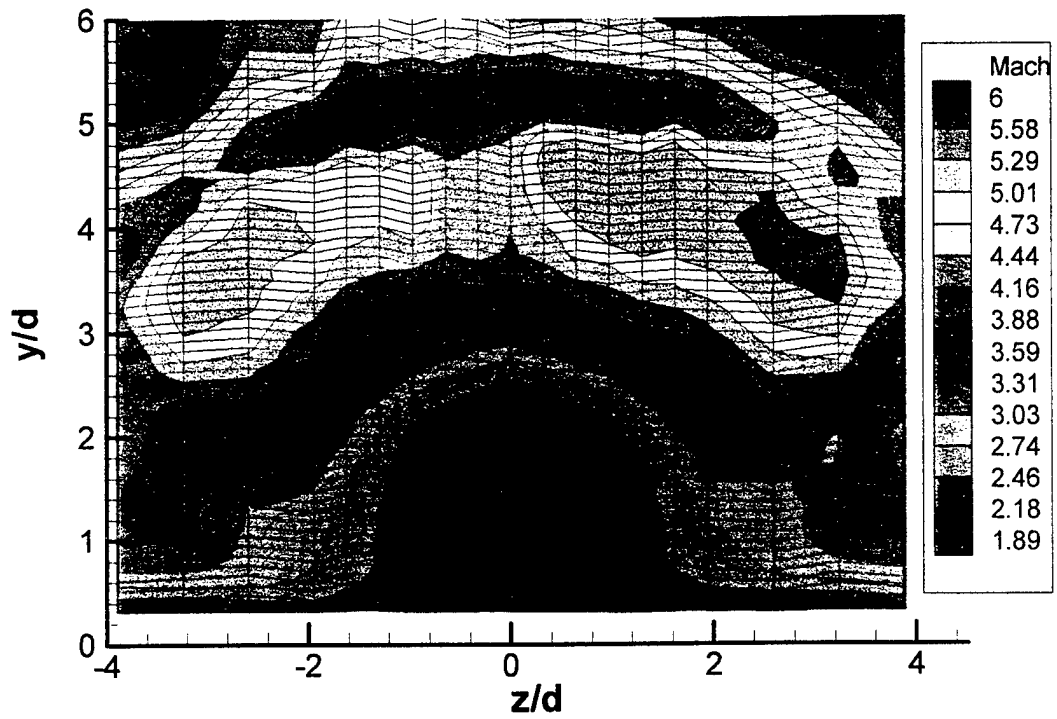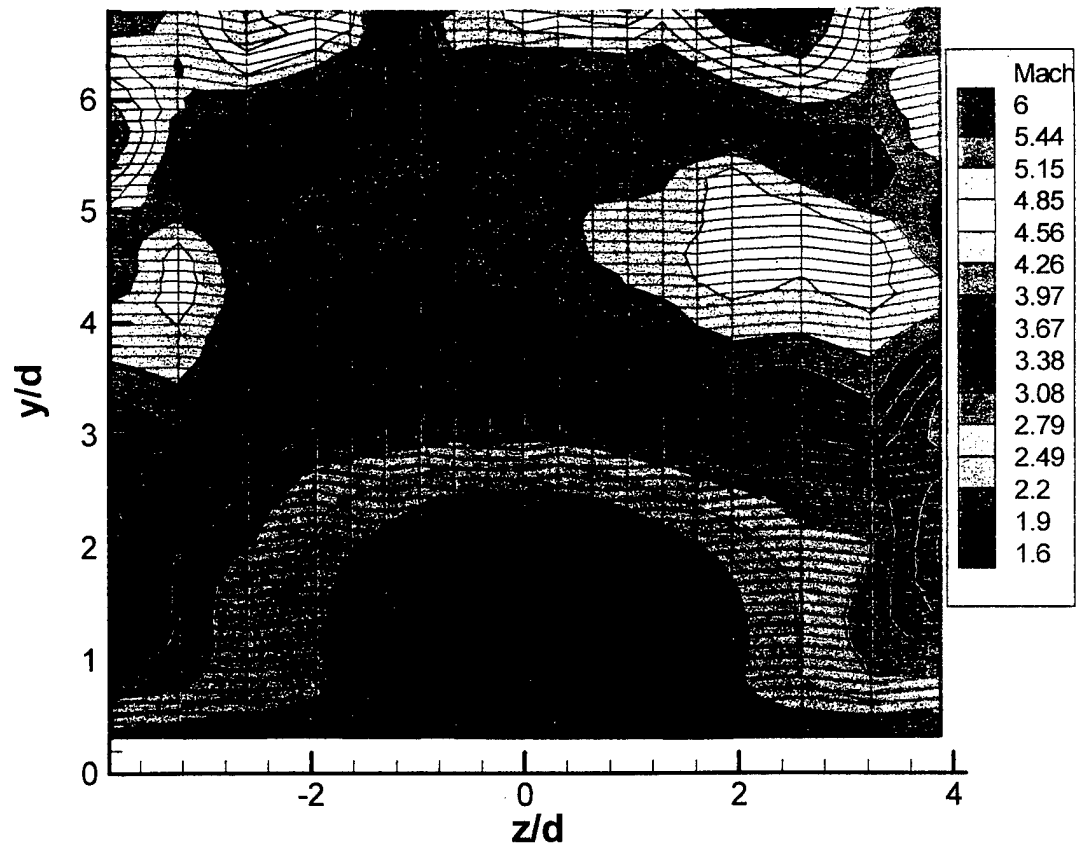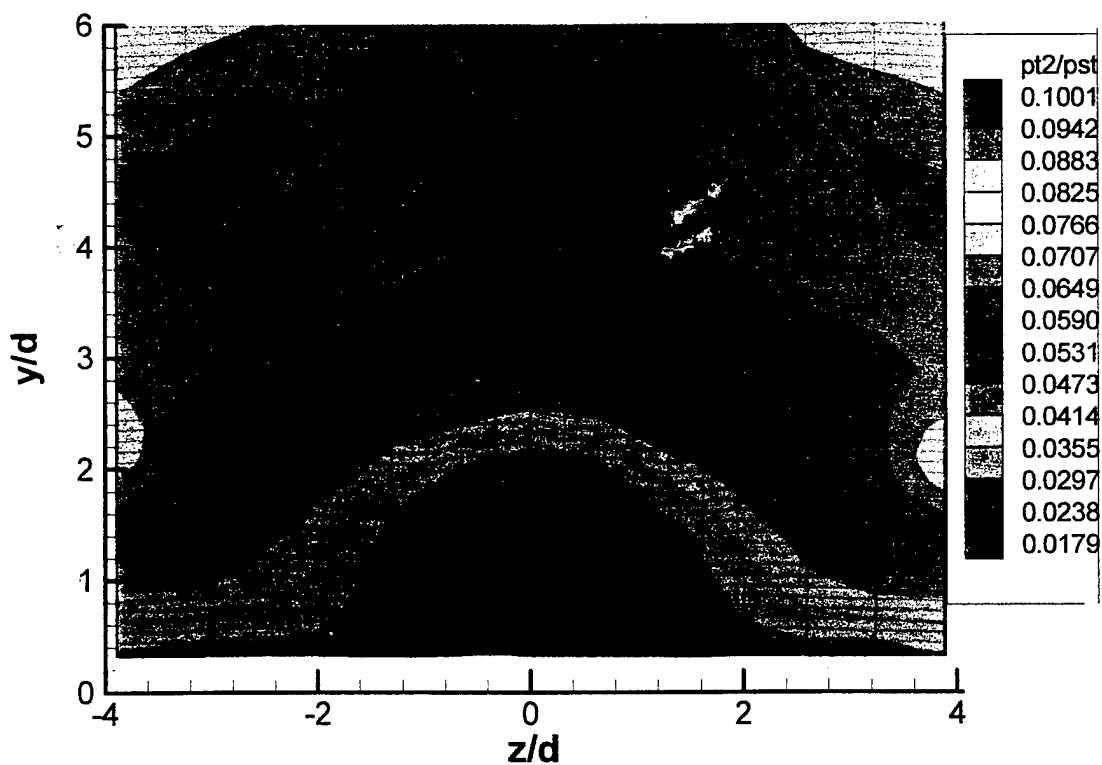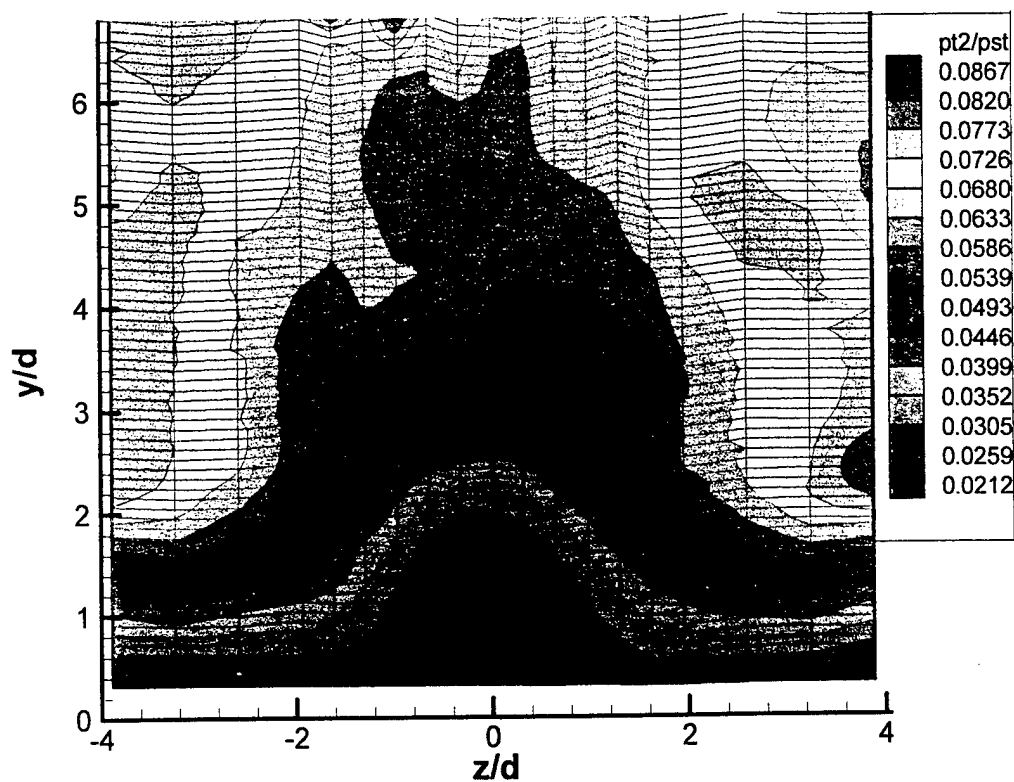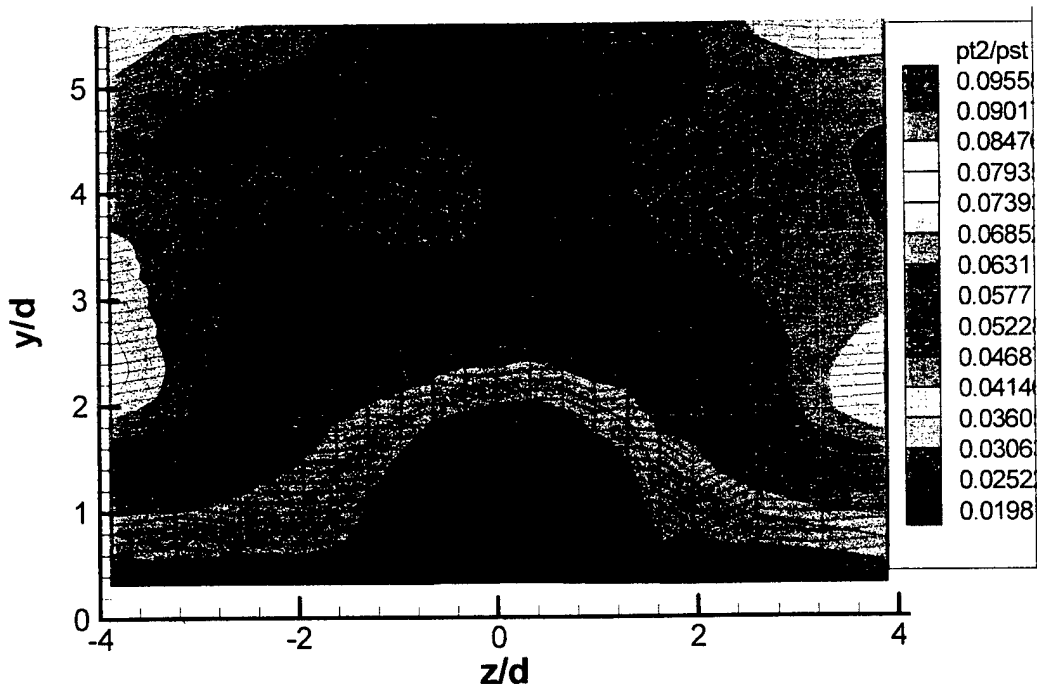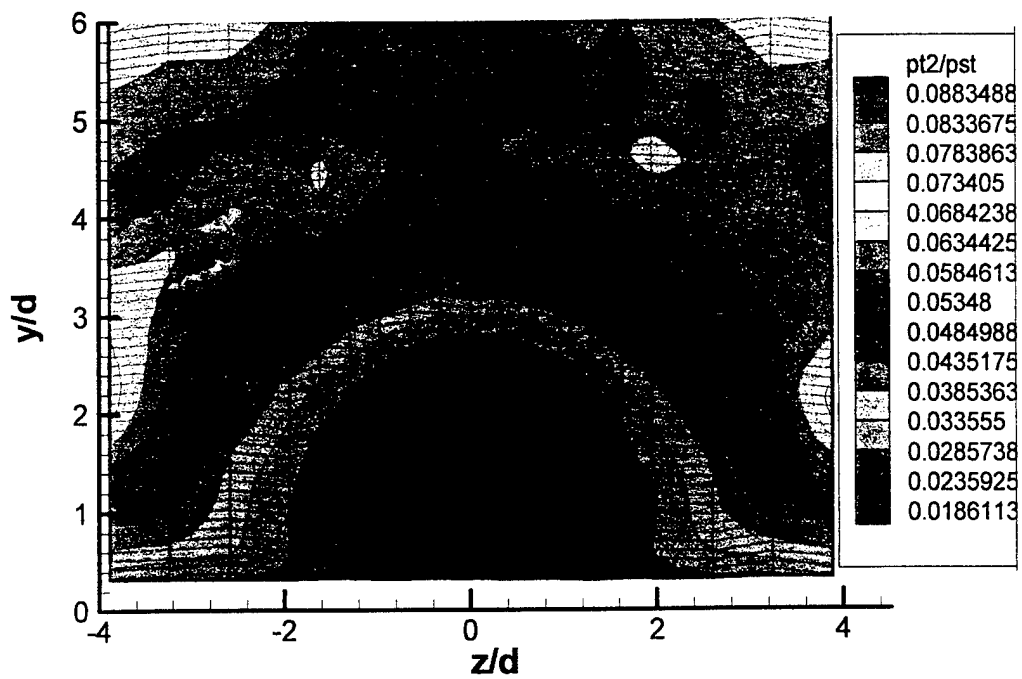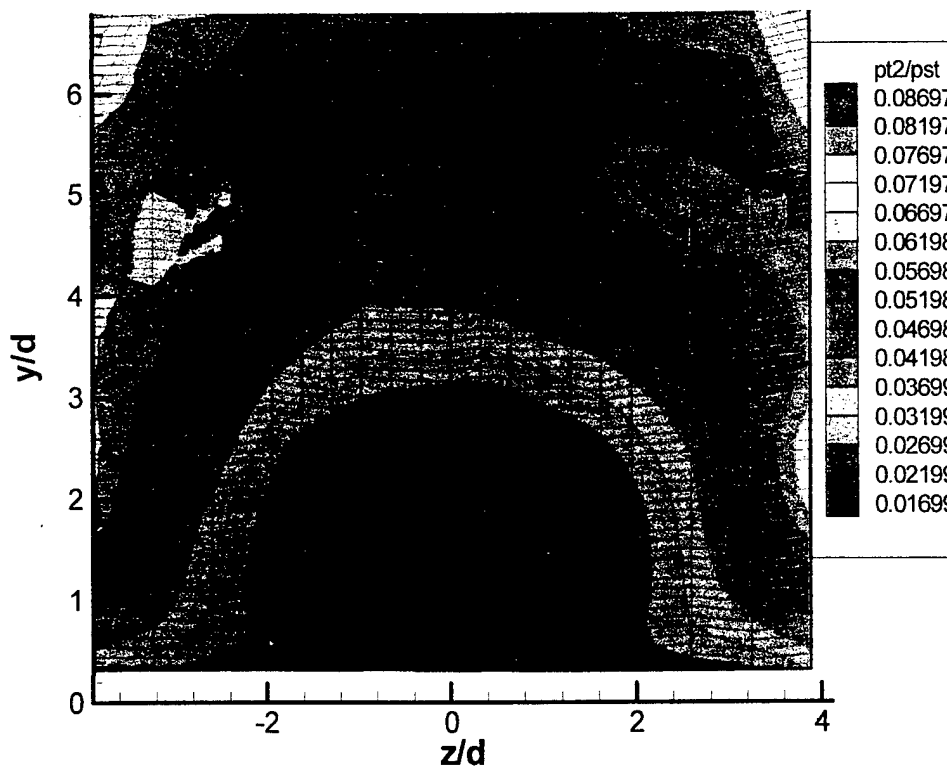
(g) 45° Diamond ($J = 1.91$)

(h) 90° Diamond ($J = 1.91$)
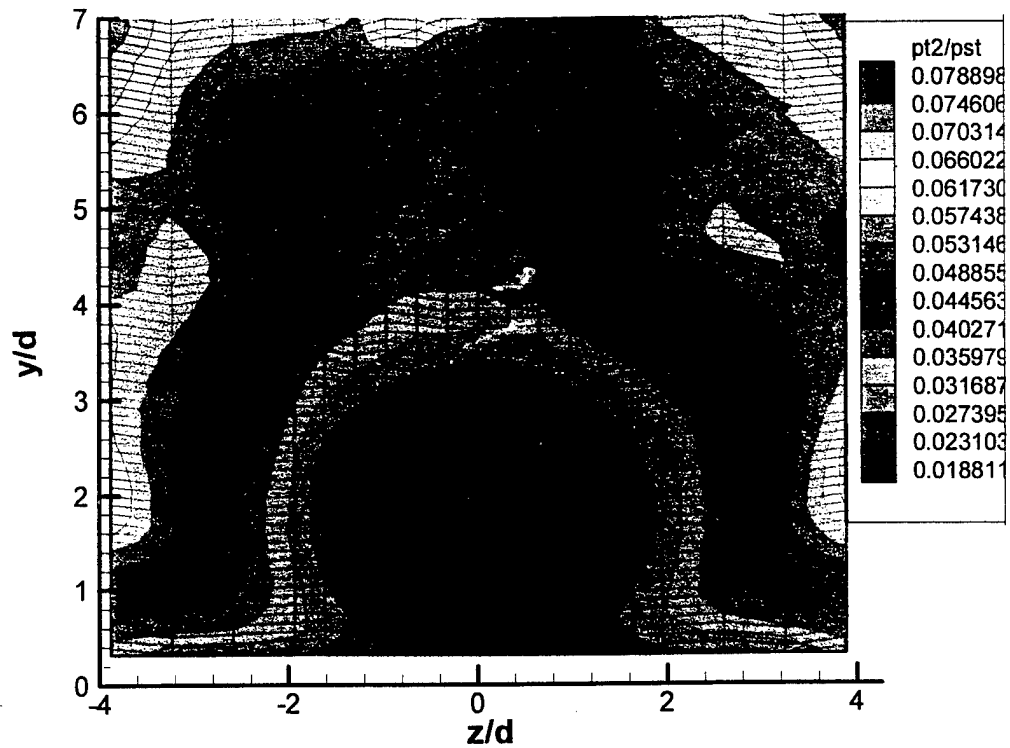
(i) 90° Circular ($J = 1.91$)
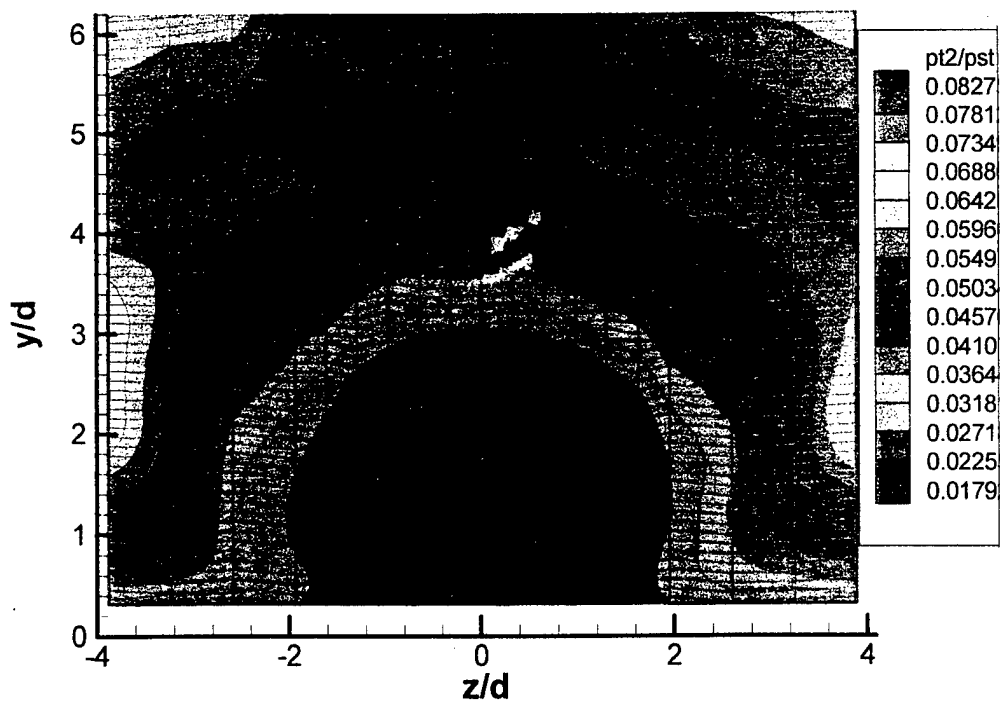
(j) 45° Diamond ($J = 2.59$)

Fig. 4.5 Pitot-Pressure Ratio ($P_{t2}/P_{t\infty}$) Contours for the Single-Port Injectors
($x/d = 21$)

10°	**27.5°**	**45°**	**90°**	**90°**

0.0 0.5 1.0 1.5 2.0 2.5

PSIA
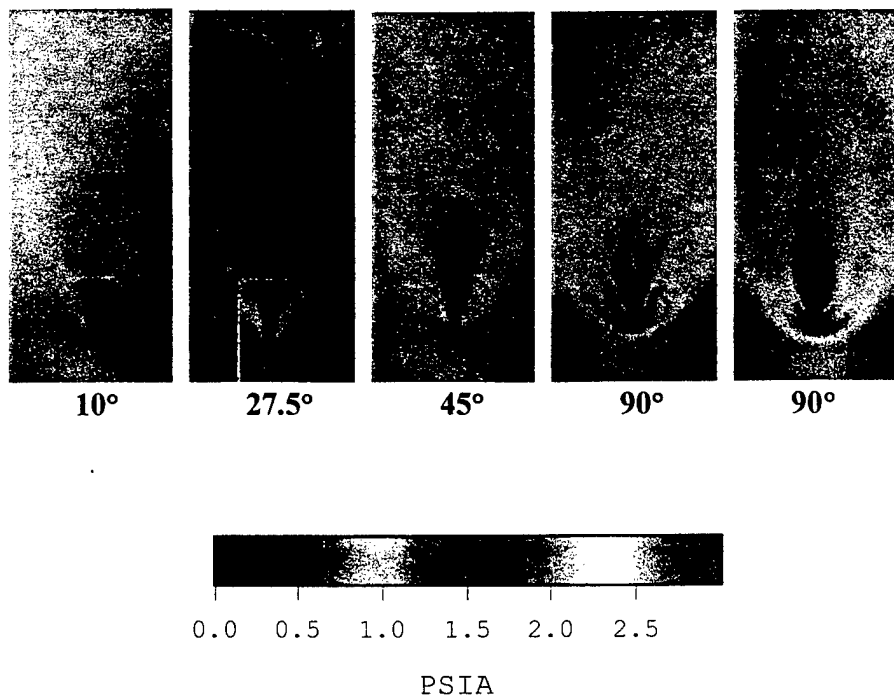
Fig. 4.6 Pressure Sensitive Paint Results
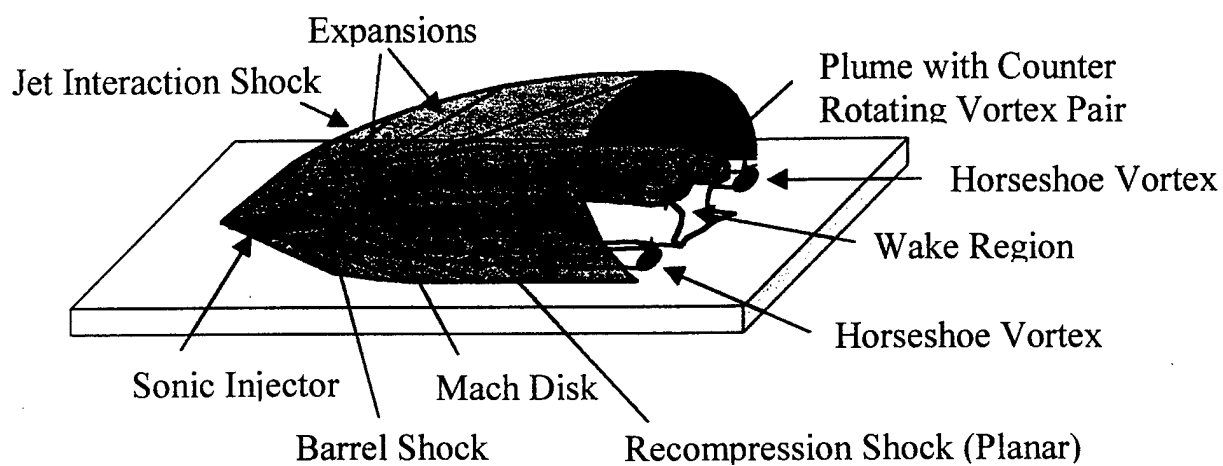
Fig. 4.7 Schematic of the Flow Field for Single-Port Jet-Interaction with Attached Jet-Interaction-Shock
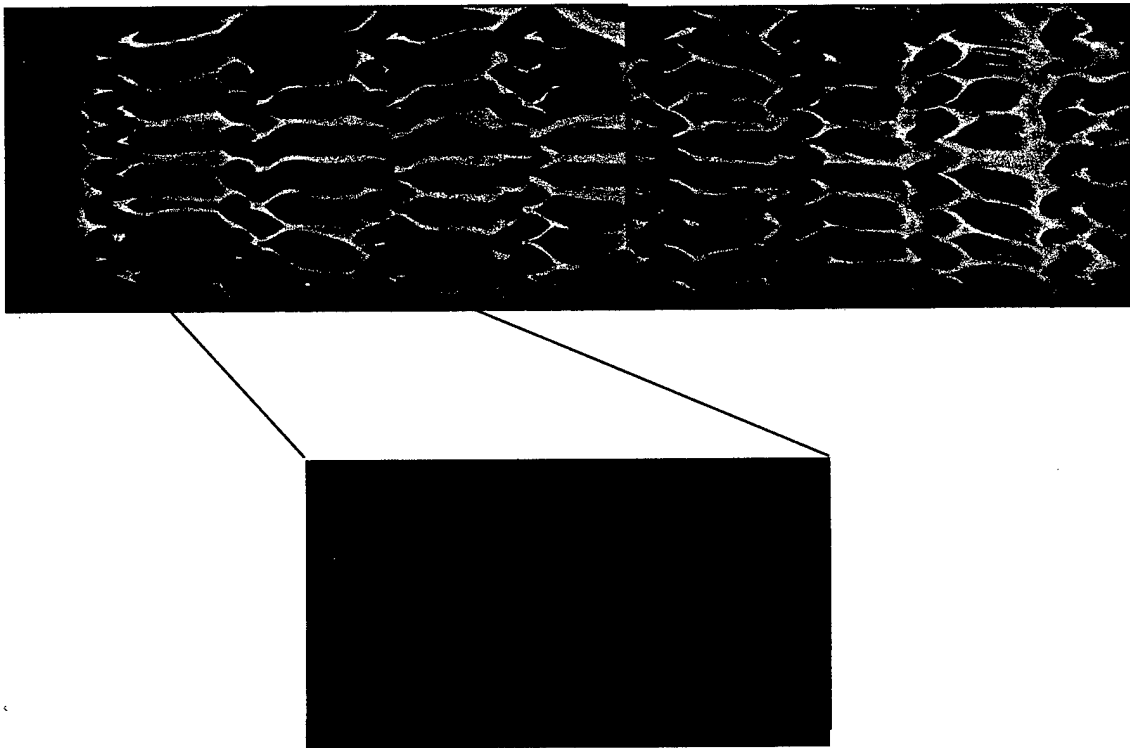
Fig. 4.8 Surface Oil Flow and Color Schlieren Flow Visualization Results for the
Distributed Array Injector
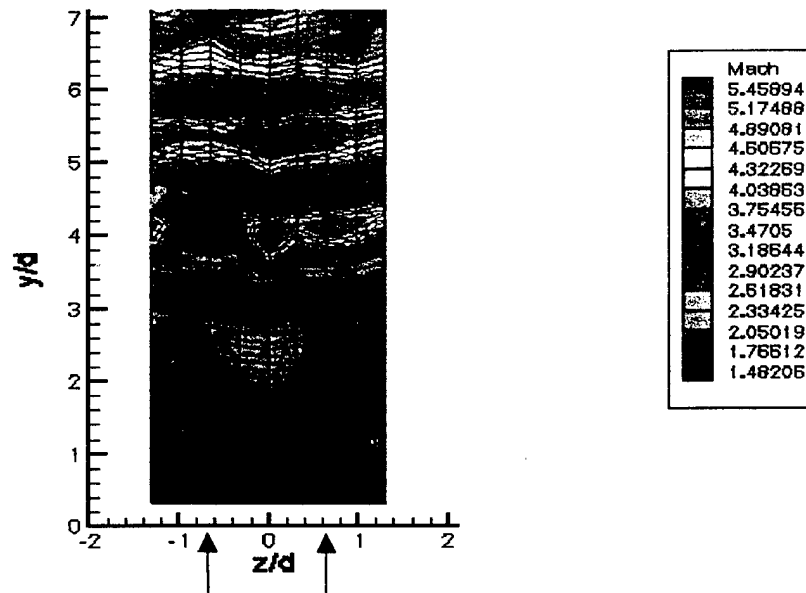
(a) Mach Number
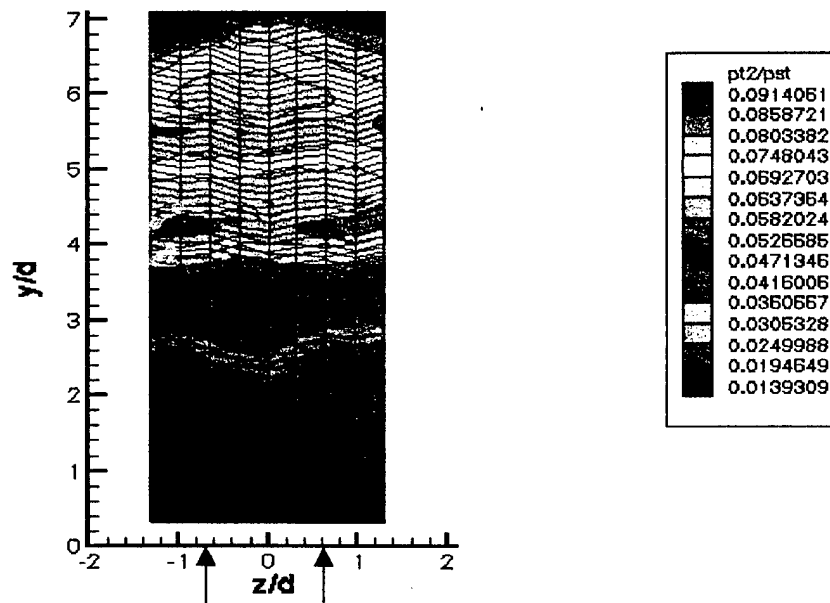
(b) $P_{t2}/P_{t\infty}$

Fig. 4.9 Five-Hole Probe Data for the Distributed Array Injector (Measurements were acquired at a location midway between axial rows 6 and 7, and arrow indicate location of two span jet rows within measurement domain.).
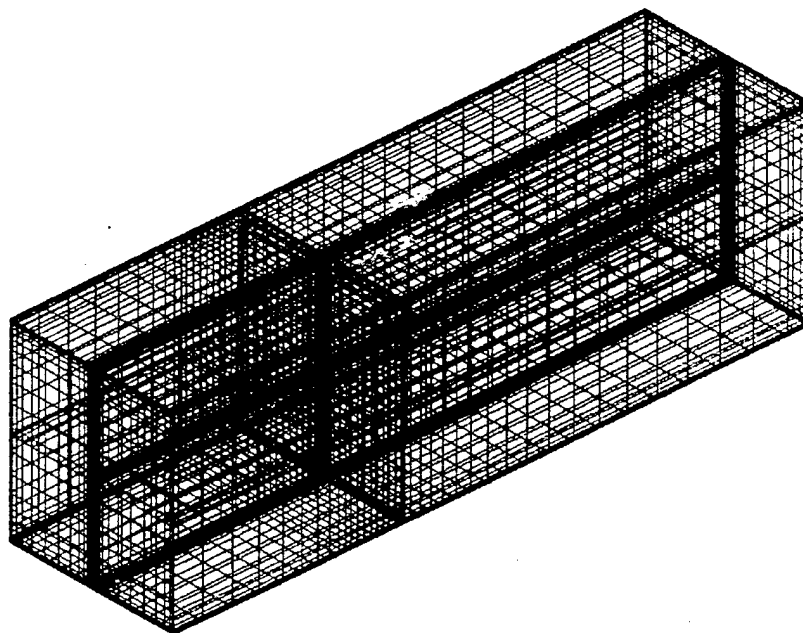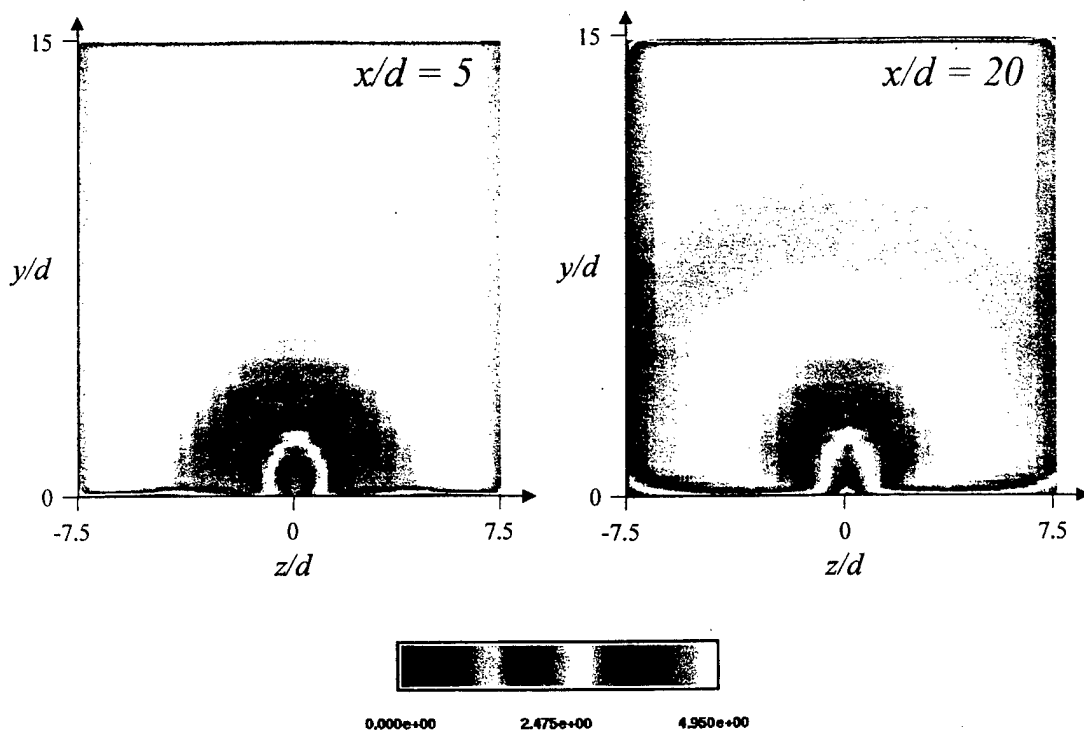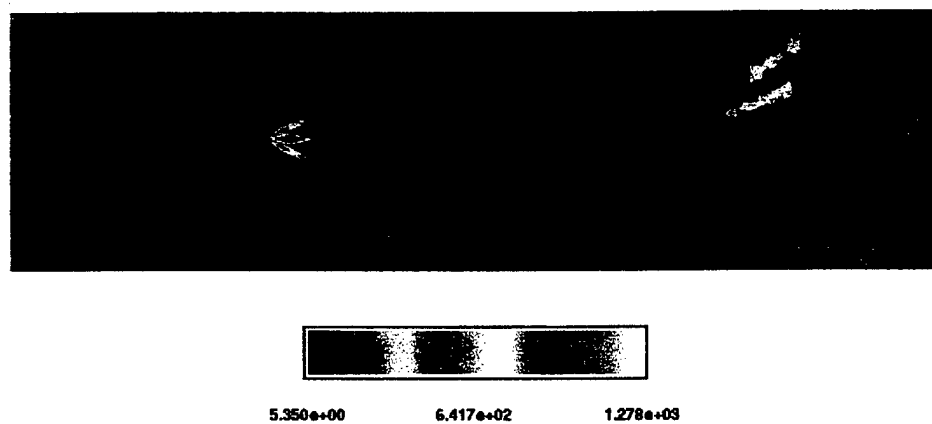
(a) Full Grid
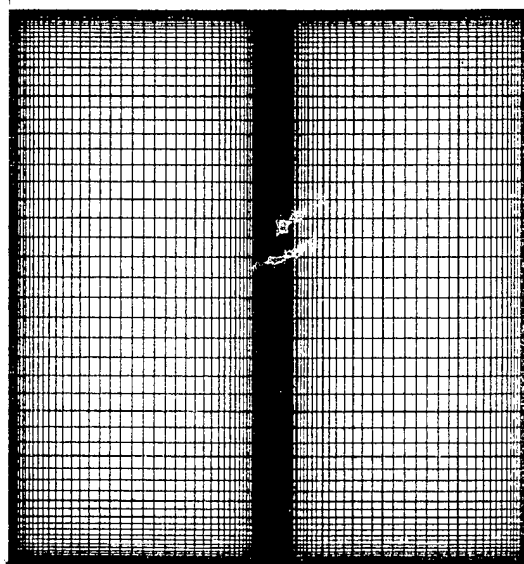
(b) Grid Cross Section (7.62 x 7.62 cm^2)

Fig. 4.10 Grid for Baldwin-Lomax Simulation (Length in x, y, and z = 25.4 cm^3, 7.62 cm and 7.62 cm, respectively. Number of grid points in the x, y and z-direction = 257, 65, 129, respectively).
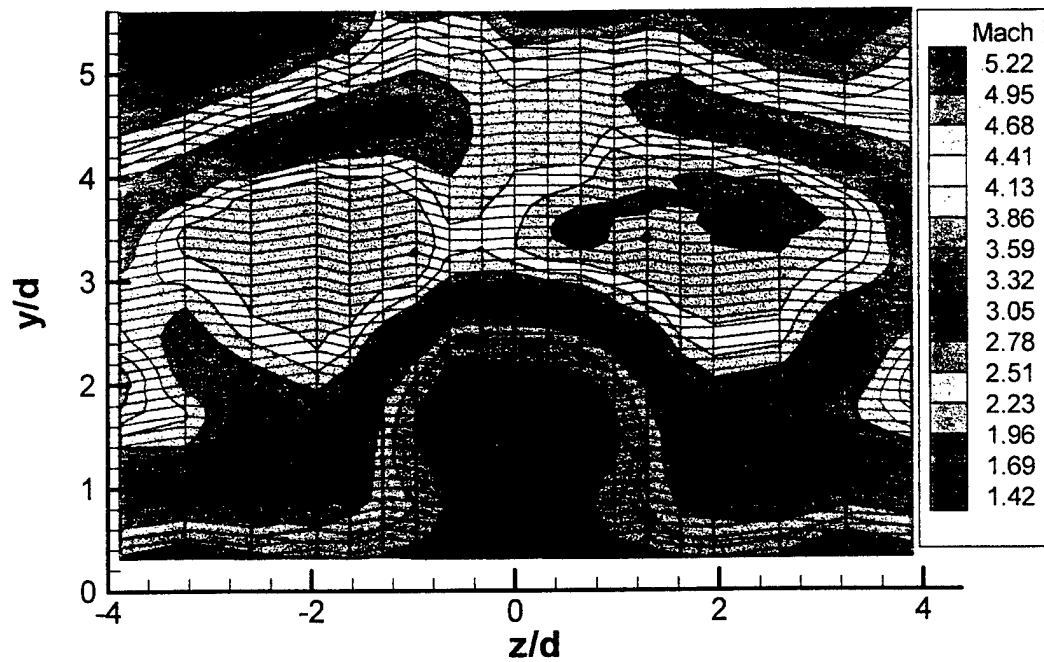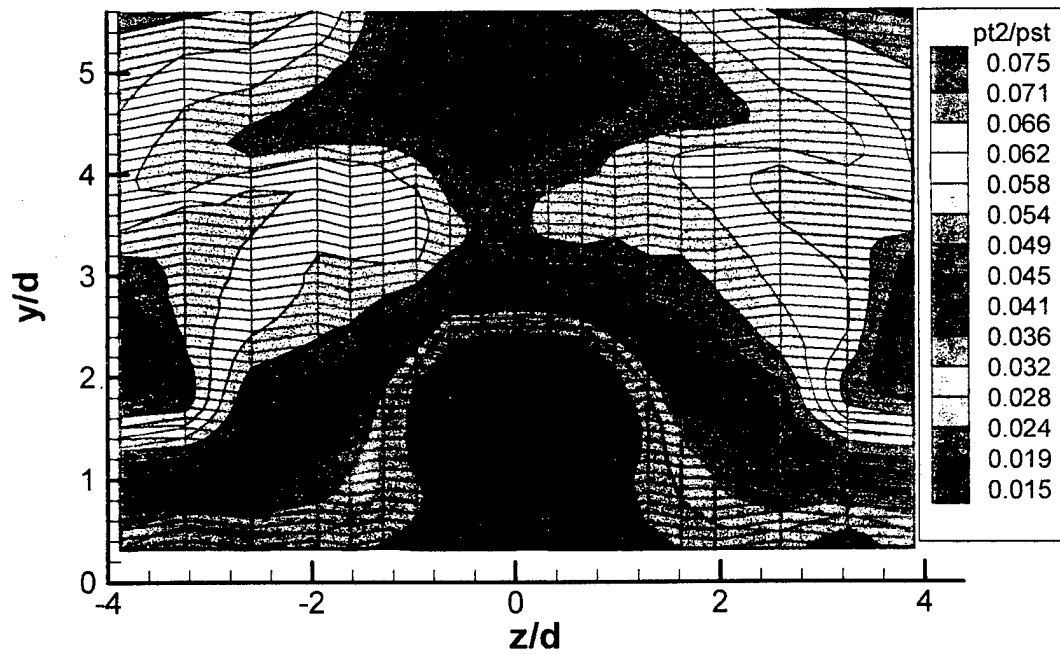
(a) Mach Number Contours

(c) Surface Pressure Distribution (lb/ft^2)

Fig. 4.11 Numerical simulation results for the 90° Diamond Injector with the Baldwin
Lomax Turbulent Model.

(a) Mach Number

(b) Pitot Pressure

Fig. 4.12 Mach Number and Pitot-Pressure Ratio ($P_{t2}/P_{t\infty}$) Contours for the 45° Single-Port Diamond Injector with the Tapered Ramp ($x/d = 21$)